

A NEW CEPHEID DISTANCE TO THE MASER-HOST GALAXY NGC 4258
AND ITS IMPLICATIONS FOR THE HUBBLE CONSTANT¹

L. M. MACRI²

National Optical Astronomy Observatory and
950 North Cherry Ave., Tucson, AZ 85719, USA

K. Z. STANEK

Department of Astronomy, The Ohio State University and
140 West 18th Ave., Columbus, OH 43210, USA

D. BERSIER

Astrophysics Research Institute, Liverpool John Moores University and
Twelve Quays House, Egerton Wharf, Birkenhead CH41 1LD, England

L. J. GREENHILL

Harvard-Smithsonian Center for Astrophysics and
60 Garden St., Cambridge, MA 02138, USA

AND

M. J. REID

Harvard-Smithsonian Center for Astrophysics and
60 Garden St., Cambridge, MA 02138, USA

ABSTRACT

We present initial results from a time-series BVI survey of two fields in NGC 4258 using the Advanced Camera for Surveys onboard the Hubble Space Telescope. This galaxy was selected because of its accurate maser-based distance, which is anticipated to have a total uncertainty of $\sim 3\%$. The goal of the HST observations is to provide an absolute calibration of the Cepheid Distance Scale and to measure its dependence on chemical abundance (the so-called "metallicity effect").

We carried out observations of two fields at different galactocentric distances with a mean abundance difference of 0.5 dex. We discovered a total of 281 Cepheids with periods ranging from 4 to 45 days (the duration of our observing window). We determine a Cepheid distance modulus for NGC 4258 (relative to the LMC) of $\Delta\mu_0 = 10.88 \pm 0.04$ (random) ± 0.05 (systematic) mag. Given the published maser distance to the galaxy, this implies $\mu_0(LMC) = 18.41 \pm 0.10_r \pm 0.13_s$ mag or $D(LMC) = 48.1 \pm 2.3_r \pm 2.9_s$ kpc. We measure a metallicity effect of $\gamma = -0.29 \pm 0.09_r \pm 0.05_s$ mag dex⁻¹. We see no evidence for a variation in the slope of the Period-Luminosity relation as a function of abundance.

We estimate a Hubble Constant of $H_0 = 74 \pm 3_r \pm 6_s$ km s⁻¹ Mpc⁻¹ using a recent sample of 4 well-observed type Ia SNe and our new calibration of the Cepheid Distance Scale. It may soon be possible to measure the value of H_0 with a total uncertainty of 5%, with consequent improvement in the determination of the equation of state of dark energy.

Subject headings: Cepheids — distance scale — galaxies: individual (NGC 4258)

1. INTRODUCTION

During the last 15 years, the *Hubble Space Telescope* (*HST*) has been used to discover $\sim 10^3$ Cepheid variables in ~ 30 galaxies with $D \lesssim 25$ Mpc, mostly through *V*- and *I*-band observations carried out with the WFPC2 instrument. The distance moduli to these galaxies have been determined through the use of a fiducial Cepheid Period-Luminosity relation (P-L) based on observations of variables located in the Large Magellanic Cloud. Several secondary distance indicators (such as type Ia SNe, the Tully-Fisher relation, the Surface Brightness Fluctuation method) have been calibrated based on these Cepheid distances. As a result of these investigations, there is some agreement that H_0 is about 70 km s⁻¹

Mpc⁻¹, perhaps with as little as 10% uncertainty (Freedman et al. 2001). However, two significant sources of systematic error stand out.

First, the entire Cepheid Distance Scale is underpinned by the distance to the Large Magellanic Cloud (LMC). The distance to that galaxy is used to establish the absolute calibration of the Cepheid P-L relations, and its uncertainty dominates the calibration of any secondary distance indicator. The suitability of the LMC for this purpose is problematic, since independent estimates of its distance disagree by as much as 0.5 mag, or 25% (Benedict et al. 2002). Additionally, the internal structure of the galaxy along the line of sight remains poorly understood (Nikolaev et al. 2004; van der Marel 2001). Faced with this situation, most Cepheid-based determinations of H_0 have adopted $\mu_{LMC} = 18.5 \pm 0.1$ mag, which corresponds to a distance of $D_{LMC} = 50.1 \pm 2.3$ kpc.

Second, the effect of metal abundance on the Cepheid P-L relation is controversial. Several independent meth-

¹ Based on observations with the Advanced Camera for Surveys onboard the NASA/ESA Hubble Space Telescope, obtained at STScI, which is operated by AURA, Inc., under NASA contract NAS 5-26555. These observations are part of program # GO-9810.

² Hubble Fellow & Goldberg Fellow

ods for an observational determination have yielded a variety of results (Sasselov et al. 1997; Kochanek 1997; Kennicutt et al. 1998; Sakai et al. 2004) with the *opposite sign* to what has been predicted by some theoretical investigations (Fiorentino et al. 2002), which also suggest a sensitivity to helium as well as metal content. Furthermore, the use of V and I photometry alone in previous HST surveys makes it difficult to disentangle the effects of reddening and metallicity and adds uncertainty to the determination of Cepheid distances.

We wish to establish a new Cepheid Distance Scale anchor galaxy, NGC 4258, for which accurate geometric estimates of distance are available. Herrnstein et al. (1999) estimated its distance modulus to be $29.29 \pm 0.09_r \pm 0.12_s$ mag, and it is anticipated that Humphreys et al., (in prep.) will reduce the total uncertainty of that estimate to $\lesssim 3\%$. Our goal is even more compelling in light of the recent *WMAP* results (Spergel et al. 2006) because many cosmological parameters depend sensitively on H_0 (e.g. Eisenstein & White 2004; Tegmark et al. 2004; Hu 2005). An accurate geometric distance to NGC 4258 can also be used to directly calibrate secondary distance indicators, such as the tip of the red giant branch (TRGB).

This paper contains the first results of our project: deep time-series BVI photometry of two fields in NGC 4258 and the discovery and analysis of Cepheid variables. The paper is organized as follows: §2 contains details of the observations, data reduction and photometry, and the search for variables; §3 describes the selection criteria and the Cepheid samples; §4 presents the determination of a Cepheid distance to NGC 4258, a measurement of the metallicity dependence of Cepheid-based distances, and a discussion of our results.

Throughout the paper, we denote random (statistical) uncertainties with a subscript r and systematic uncertainties with a subscript s , i.e., $\pm 0.10_r \pm 0.10_s$ mag.

2. OBSERVATIONS, DATA REDUCTION AND PHOTOMETRY

2.1. Observations

We used the *Hubble Space Telescope* (GO program 9810) to observe two fields located at widely different galactocentric radii within the disk of NGC 4258 (M106). This spiral galaxy is one of the brightest members of the Coma-Sculptor Cloud (Tully & Fisher 1987), and has been classified as SAB(s)bc II-III (de Vaucouleurs et al. 1991) and Sb(s) II (Sandage & Tammann 1987).

We carried out the observations using the Advanced Camera for Surveys / Wide Field Camera (Ford et al. 2003), which consists of 2 back-illuminated SITE 2048 \times 4096 pixel CCDs. The average plate scale of the focal plane is $0''.05 \text{ pix}^{-1}$, making each image $\sim 202''$ on the side. At the nominal NGC 4258 distance of ~ 7.2 Mpc, this translates to a physical size of $\sim 1.7 \text{ pc pix}^{-1}$.

Hereafter, we refer to the two fields based on their galactocentric radii as “inner” and “outer”. The fields are centered at $(\alpha, \delta) = 12^{\text{h}}18^{\text{m}}47.518^{\text{s}}, +47^{\circ}20'20''.10$ (inner) and $12^{\text{h}}19^{\text{m}}23.891^{\text{s}}, +47^{\circ}11'37''.61$ (outer), in J2000.0 coordinates. Figure 1 shows the location of these fields in the context of a digitized POSS-II image of NGC 4258³.

The fields were observed on twelve separate epochs between 2003 December 5 and 2004 January 19. The spacing of the visits followed a power-law distribution to minimize aliasing (Madore & Freedman 2005). Table 1 contains a log of the observations. The fields were imaged in three colors on two consecutive orbits during each visit, following a standard two-point dither pattern that minimizes the effects of the geometric distortion present in ACS while ensuring a robust cosmic-ray rejection. Total exposure times per epoch were $2 \times 900s$ using the $F435W$ filter (similar to Johnson B), $2 \times 800s$ using the $F555W$ filter (similar to Johnson V) and $2 \times 400s$ using the $F814W$ filter (similar to Kron-Cousins I). One of the visits to the outer field was hampered by guide-star problems, reducing the total number of useful images by one relative to the inner field.

2.2. Data Reduction and Photometry

The raw observations were processed by the standard on-the-fly-reprocessing STScI ACS calibration pipeline, as described in the ACS Data Handbook (Pavlovsky et al. 2005). Briefly, the pipeline performs bias level correction and subtraction, dark image subtraction, flat fielding correction, and generation of ancillary data quality information. The calibrated images were downloaded from the STScI Archive and further processed using STSDAS and PyRAF⁴. Specifically, we used the PyDrizzle task to apply the filter-dependent geometric distortion correction to individual images.

We performed PSF photometry using the DAOPHOT/ALLSTAR/ALLFRAME suite of programs (Stetson 1987, 1994) and following the general data reduction and analysis precepts of the HST Key Project on the Extragalactic Distance Scale (e.g., Stetson et al. 1998). All the programs whose names appear in CAPITALS were developed and kindly provided to us by Peter Stetson.

We defined the PSF as a quadratically-varying Moffat function with $\beta = 1.5$ and a fitting radius of 2 pixels. The PSF extended out to a radius of 10 pixels ($0''.5$) and the local sky annulus was established from 20 to 25 pixels ($1 - 1''.25$). Aperture photometry was measured at logarithmically spaced radii from 3 to 10 pixels.

2.2.1. Determination of template PSFs

As expected in extragalactic Cepheid observations, our fields are rather crowded and lack bright, isolated stars suitable for the determination of the point-spread function (PSF). Given the long-term stability of *HST*, it is feasible to determine suitable PSFs from high S/N observations of dense yet uncrowded stellar fields. To this end, we retrieved a observations of an outer field of the globular cluster NGC 104 (program 9018), originally obtained for calibration purposes, from the HST Archive.

We analyzed 18 images in each of the $F435W$, $F555W$ and $F814W$ filters, taken at various offset positions. We used ~ 800 bright stars present in all the images to derive

from NSF, NASA, the National Geographic Society, the Sloan Foundation, the Samuel Oschin Foundation, and the Eastman Kodak Corporation. The Oschin Schmidt Telescope is operated by the California Institute of Technology and Palomar Observatory. The Digitized Sky Survey was produced at the Space Telescope Science Institute under U.S. Government grant NAG W-2166.

⁴ STSDAS and PyRAF are products of the Space Telescope Science Institute, which is operated by AURA for NASA

³ The Second Palomar Observatory Sky Survey (POSS-II) was carried out by the California Institute of Technology with funds

the PSF for each filter and to map its positional variation across the field of view of ACS/WFC. This was achieved using MULTIPSF, which is identical to the PSF routine in DAOPHOT but uses stars in multiple images.

2.2.2. PSF photometry

We carried out PSF photometry separately for each combination of field and filter, as follows:

1. Image registration & master image: We used DAOPHOT to detect bright stars in the individual images and ALLSTAR to perform preliminary PSF photometry and obtain accurate coordinates of those objects. We used DAOMASTER to determine coordinate transformations for every image, taking as reference the first image of each set. We used MONTAGE to create a “master” image by interpolating the individual frames and applying a median filter. Figures 2 & 3 are color composites of the ACS fields, created from the master *BVI* images.

2. Master object lists: We detected objects in the master image following a two-step iterative approach (detect all objects, subtract them from the image, detect all remaining objects and add them to the initial list). At each iteration, we required a 3σ detection. The total number of objects detected were $\sim 2, 3$ and 6×10^5 in *BVI*, respectively, for the inner field and $\sim 0.6, 1$ and 2×10^5 in *BVI*, respectively, for the outer field.

3. PSF Photometry: We used ALLFRAME to measure the magnitudes of every star in each master list across all individual images in a given field/filter combination. We used the same template PSFs (§2.2.1) for all frames in a given filter. This generated a total of $\sim 2.3 \times 10^7$ photometric measurements.

4. Secondary standards: We searched the star lists for bright, isolated stars suitable to serve as secondary standards. We identified $\sim 30 - 50$ suitable stars depending on the field and filter. We subtracted all other objects from each individual image and performed aperture photometry on these secondary standards to generate curves of growth. These were analyzed using DAOGROW (Stetson 1990) and compared to the curves of growth determined from bright, isolated stars in NGC 104. We found no difference between the two sets and decided to use both in our analysis.

5. Growth curves: We used COLLECT to apply the curves of growth and determine aperture corrections using the secondary standards. The corrections were small, with average values of $+0.02 \pm 0.04$, -0.04 ± 0.03 , -0.05 ± 0.02 mag in *BVI*, respectively. Epochs #10 and #11 had substantially larger aperture corrections (~ 0.2 mag), probably due to telescope de-focusing.

6. Zeropoints: We used CCDAVE to compute mean instrumental magnitudes for the secondary standards. A typical r.m.s. scatter for these stars was 0.035 mag, and as low as 0.015 mag for the brightest objects. We used TRIAL to compute the final zero-point corrections for each frame, using as a reference the mean aperture-corrected instrumental magnitudes of the secondary standards.

7. Astrometry: We calculated celestial coordinates for all objects using the WCSTools/xy2sky program (Mink 2002) and the astrometric solutions provided by STScI in the FITS headers of the first *F555W* image of each field.

2.3. Photometric calibration

As a first step in our photometric calibration, we corrected the instrumental magnitudes for the effect of charge transfer efficiency (CTE) by applying Eqn. (2) of the ACS Instrument Status Report 04-06 (Riess & Mack 2004). We used the parameters derived by those authors for an aperture of 3 pixels in radius, since that is similar to the effective radius of the PSF for the bandpasses of interest (A. Riess, priv. comm.). Given the appreciable sky background in both inner and outer fields, the CTE correction was fairly small (~ 0.02 mag).

We calibrated our photometry following the procedures of Appendix B of Sirianni et al. (2005), using the zero-points and color terms listed under the “observed” columns of their Table 22:

$$V = F555W - AC05_V + 25.704 - 0.054(V - I) \quad (1a)$$

$$V = F555W - AC05_V + 25.701 - 0.056(B - V) \quad (1b)$$

$$I = F814W - AC05_I + 25.495 - 0.002(V - I) \quad (2)$$

$$B = F435W - AC05_B + 25.842 - 0.089(B - V) \quad (3)$$

where *BVI* are the standard magnitudes and *F435W*, *F555W*, *F814W* are the CTE-corrected, aperture-corrected (to $0''.5$) instrumental magnitudes derived in §2.2.2. The additional filter-dependent aperture corrections to infinity, $AC05_i$, are listed in Table 5 of Sirianni et al. (2005). In the case of objects with three-color photometry (such as all the Cepheid variables), we gave preference to (1a) over (1b) because our *I*-band observations have higher *S/N* than our *B*-band observations. Since these transformation equations make use of the standard (rather than observed) colors, they were applied iteratively until convergence.

Table 2 lists the positions and calibrated magnitudes of the secondary standards to facilitate future comparisons with our work.

2.4. Search for Variables and Classification

We searched for variables using the TRIAL program, which performs a scaling of the reported ALLFRAME measurement errors and calculates robust mean magnitudes and modified Welch-Stetson variability indices L_V (Stetson 1996). Figure 4 shows the distribution of L_V as a function of *V* magnitude for the outer field (the inner field distribution is very similar but denser). By construction, the mean value of L_V is zero. Given the observed 1σ dispersion in L_V of 0.25, we set $L > 0.75$ as the minimum variability threshold. We calculated the twenty most likely periods for each variable using the Lafler-Kinman algorithm (Lafler & Kinman 1965) as encoded in TRIAL.

We applied an automated classification algorithm developed by the DIRECT project (Kaluzny et al. 1998) to the *V*-band light curves of the variables. The algorithm computed the chi-squared per degree of freedom, χ^2_ν , of each light curve for three cases: i) a constant magnitude (null hypothesis); ii) a linearly-varying magnitude (appropriate for objects with periods much longer than our observing window); iii) a Cepheid variable with a period equal to each one of the twenty tentative periods returned by the Lafler-Kinman algorithm. The latter case used the Cepheid template light curves developed by Stetson (1996).

We selected as possible Cepheids those periodic variables with a χ^2_ν for case (iii) that was at least a factor of two smaller than the χ^2_ν of cases (i) or (ii), following the methodology of the DIRECT project. Adopting the best-fit period, we phased the B - and I -band light curves and fit them with Cepheid template light curves (absent B -band templates, we used suitably scaled V -band ones). Finally we phase-weighted mean magnitudes (Stetson 1996) through numerical integration of the best-fit template light curve for each variable.

3. SELECTION OF CEPHEID VARIABLES

3.1. Adopted Period-Luminosity relations

Our analysis requires the adoption of fiducial Period-Luminosity (P-L) relations to calculate distance moduli, as well as corresponding Period-Color (P-C) relations to correct for the effects of interstellar extinction. We adopted the P-L relations originally derived by Udalski et al. (1999), as updated in the OGLE web site⁵. These relations are based on a sample of $N > 600$ Cepheids observed as part of the OGLE II project, with periods ranging from 2 to 30 days:

$$B = 14.929(31) - 2.439(46) [\log P - 1] \quad (4)$$

$$V = 14.287(21) - 2.779(31) [\log P - 1] \quad (5)$$

$$I = 13.615(14) - 2.979(21) [\log P - 1] \quad (6)$$

where P is the period of the Cepheid in days, and the errors in the zero-points and slopes are expressed in units of 10^{-3} . The dispersions of the data relative to the relations are 0.24, 0.16 and 0.11 mag in BVI , respectively.

3.2. Extinction corrections and relative distance moduli

NGC 4258 is located at $l = 138^\circ 32'$, $b = 68^\circ 84'$. We estimated the value of foreground Galactic interstellar extinction based on the values in the reddening map of Schlegel et al. (1998) for a number of positions near the galaxy. All of them yielded very low values of foreground extinction, $E(B - V) = 0.016$ mag. We expect little additional (internal) extinction in the outer field, but the Cepheids in the inner field should be subject to a considerably larger amount of internal extinction with strong variations as a function of position.

We determined the total extinction to each Cepheid by comparing the observed $B - V$, $V - I$ and $B - I$ colors with the zero-extinction colors $(B - V)_0$, $(V - I)_0$ and $(B - I)_0$ predicted by the P-C relations formed by Eqns. (4-6). We transformed the values of $E(V - I)$ and $E(B - I)$ to $E(B - V)$ using the values of A_λ from Table 6 of Schlegel et al. (1998) for $R_V = 3.1$ and the extinction law of Cardelli et al. (1989). We used the three color excesses to compute a mean $E(B - V)$ and standard deviation, but adopted a 0.025 mag uncertainty floor to account for the intrinsic width of the P-C relations.

We determined extinction-corrected LMC-relative distance moduli for each Cepheid by calculating:

$$\Delta\mu_0 = \Delta\mu_I - 1.45E(V - I) \quad (7)$$

$$\Delta\mu_0 = \Delta\mu_I - 2.38E(B - I) \quad (8)$$

$$\Delta\mu_0 = \Delta\mu_I - 1.94E(B - V) \quad (9)$$

where $\Delta\mu_I$ is obtained by subtracting the mean value of $I(P)$ from Eq. (6) from the mean I -band magnitude of a given Cepheid of period P . The values of total-to-selective extinction ratios were calculated using the $A_\lambda/E(B - V)$ values in Table 6 of Schlegel et al. (1998). The three values of $\Delta\mu_0$ were averaged to obtain a mean value and standard deviation. Eqn. (7) is the classical Wesenheit distance modulus used by Freedman et al. (2001) and Saha et al. (2001), although these authors apply it to distance moduli determined from an ensemble of Cepheids. We chose to form the additional two relations (Eqns. 8-9) to rule out any global systematic error in the calibration of the photometry.

We note that in this analysis, all the calculated distance moduli are *relative* to the LMC, since the adopted P-L relations are expressed in *observed* magnitudes. We adopt this approach to accommodate the anticipated improvement in the geometric distance estimate for NGC 4258 to be obtained from new analyses of the maser observations (Humphreys et al., in prep.).

3.3. Selection criteria

The selection of Cepheids from a larger set of periodic variables is not a trivial undertaking for *HST* observations, especially given the crowded nature of the fields, the sparse sampling of the light curves and the relatively low S/N of the individual data points at the faintest magnitudes (corresponding to the shortest periods). Different studies have adopted various selection techniques, some based on visual inspections of light curves and images (Saha et al. 1996) and some based on a more mathematical approach (Leonard et al. 2003).

In the case of these observations of NGC 4258—which is located significantly closer than most Cepheid-bearing galaxies studied with *HST*—it is fairly easy to select a sample of high-quality Cepheids with $P \gtrsim 10$ days for the primary scientific goals of deriving a distance and measuring the metallicity effect. The values we obtain are insensitive to the application of different selection techniques. The selection of shorter-period ($P \lesssim 10$ d) Cepheids is less certain, especially in the case of the inner field. We have adopted a particular set of selection criteria, but we list all detected Cepheid candidates to facilitate alternative analyses by others.

We restricted the sample of variables using two cuts in L_V : a fairly low value of 0.75 (hereafter, the “extended sample”) and a more conservative value of $L_V = 2$ (hereafter, the “restricted sample”). We applied additional selection criteria based on observed properties (light curve amplitude ratios, colors, etc.) in an attempt to remove contaminated Cepheids from the sample.

We detected a total of $\sim 10^6$ distinct objects at the $> 3\sigma$ level in the master images. To exclude false positives, we trimmed objects detected in less than 75% of the individual images of each band.

As stated in §2.4, variable stars were classified as Cepheids if the χ^2_ν was reduced by more than a factor of two (relative to the null hypothesis) when fitting the phased V -band data with a template Cepheid light curve. These requirements were met by 536 objects in the extended sample and 258 objects in the restricted sample. We applied the following secondary selection criteria:

1. Amplitude ratios: Relative BVI amplitudes for fundamental-mode pulsators obey the proportions 1.5 :

⁵ ftp://sirius.astrouw.edu.pl/ogle/ogle2/var_stars/lmc/cpep/catalog/README.PL

1 : 0.5. To discard obvious blue or red blends, we required (a) an I -to- V amplitude ratio of 0.5 ± 0.25 and (b) a B -to- V amplitude ratio of 1.5 ± 0.5 .

2. Blue edge: We discarded objects with $E(B-V)$ more than 2σ below the Galactic foreground value of 0.016 mag, as these variables are likely to be blended with blue stars. We set $E(B-V) = 0.016$ mag for objects between the threshold and the foreground value.

3. Large extinction: We rejected objects with $E(B-V) > 0.5$ mag. These Cepheids are either blended with red stars or highly reddened, in which case the actual value of R_V could deviate significantly from the adopted value of 3.1.

4. Pop II Cepheids: We imposed a conservative upper limit of $\Delta\mu_0 < 12$ mag to the LMC-relative distance moduli to reject long-period RV Tauri and W Virginis variables in our sample. These Population II Cepheid-like variables obey period-color relations that are similar to those of Cepheids, and therefore had passed the previous selection criteria. However, their absolute magnitudes are more than 1 mag fainter than Cepheids.

Once these cuts were applied, we computed a mean modulus for each sample using a least-absolute-deviation technique with iterative sigma clipping. This was motivated by the asymmetric tails of outliers that are caused by other sources of contamination, many of which make objects artificially brighter.

3.4. Final Cepheid samples

Table 3 details the effects of the selection criteria (§3.3) on the initial samples. 281 out of 536 variables in the extended sample pass all criteria, while 173 out of 258 variables in the restricted sample remain. Figure 5 shows the period distributions for both cuts in L_V . We used the restricted sample ($L_V > 2$) in the subsequent analysis.

The observed properties of the 281 Cepheids that passed our selection criteria are listed in Table 4, while those of the 255 rejected candidates are listed in Table 5 along with the reasons for their rejection. Table 6 lists the derived properties of the Cepheids in Table 4. Table 9 contains the individual photometric measurements of these objects.

Figures 6 & 7 show the distribution of the Cepheids within the outer and inner fields, respectively; individual finding charts can be seen in Figures 8a-g. Figures 9 & 10 show the distribution of the Cepheids within the color-magnitude diagrams of the two fields. Representative light curves are shown in Figures 11 & 12. Lastly, Figures 13 and 14 contain the observed BVI P-L relations of the restricted samples.

4. RESULTS AND DISCUSSION

4.1. The Maser Distance to NGC 4258

Water maser emission observed from NGC 4258 originates in a subparsec annular region within a nearly edge-on, warped accretion disk, bound by a supermassive black hole in the nucleus (Miyoshi et al. 1995; Greenhill et al. 1995). Masers lie: (1) in a narrow sector on the near side of the disk and (2) on the disk-diameter perpendicular to the line of sight.

Geometric estimates of distance may be obtained from measurements of the centripetal acceleration or the proper motion of masers on the near side of the disk.

The acceleration is obtained from the time rate of change of the maser Doppler shifts, and the proper motion is obtained from the change in the positions of the near-side masers relative to the approaching/receding masers (which appear to be stationary on the sky).

Herrnstein et al. (1999) reported acceleration and proper motion distance moduli that agreed to $< 1\%$: $\mu_{\text{maser}} = 29.29 \pm 0.09_r \pm 0.12_s$ mag. The quoted systematic uncertainty arises largely from unmodeled structure and an upper limit on the eccentricity of the disk. Initial models assumed circular orbits and a warp in position angle alone. More recently, Herrnstein et al. (2005) performed a detailed analysis of the disk rotation curve and detected a 2σ deviation from a Keplerian law, which they attributed to an inclination-warp in the disk. That also helps to explain the locus of the near-side masers.

Humphreys et al., (in prep.) aim to reduce the random component of the uncertainty by including more epochs of observation, and more importantly, to reduce the systematic component by improving the dynamical model of the maser-disk system. The Herrnstein et al. (1999) distance relied on VLBI data collected at four epochs between 1994 and 1997, while data for 18 VLBI epochs (1997-2000) and 40 spectroscopic epochs (1994-2003) are now available. The analysis also limited disk eccentricity to $\lesssim 0.1$. More densely sampled data with a longer time baseline, coupled with a more sophisticated model of the disk warp and eccentricity, are anticipated to reduce the systematic and random uncertainties in distance by more than a factor of two, for a total uncertainty of $\sim 3\%$ (Humphreys et al. 2005a,b).

4.2. A Cepheid distance to NGC 4258

4.2.1. Minimum period cut

We imposed minimum period cuts to the samples derived in §3.4 before we determined mean relative distance moduli. Several reasons motivate the use of such a cut.

a) We are unable to differentiate between fundamental and overtone pulsators due to our sparse phase sampling. Overtone pulsators in the Magellanic Clouds have $2 < P < 6$ days and are ~ 0.75 mag brighter than fundamental pulsators with the same period (Udalski et al. 1999). Hence, they can produce a large systematic bias in the derived distance.

b) Confusion noise introduces a systematic bias in the photometry of Cepheids that becomes increasingly important at faint magnitudes, especially in the I -band (Saha & Hoessel 1990; Saha et al. 1996).

c) Observing objects near the detection limit may result in incompleteness bias at the shortest periods of the observed P-L relation (Sandage 1988).

d) The observed magnitudes of short-period Cepheids are more likely to be contaminated by unresolved blends with other disk stars (Mochejska et al. 2000), especially in the denser regions of the inner field.

We applied the cut at minimum period and calculated the mean value of the individual relative distance moduli following the procedure described in §3.3. Figures 15 & 16 show the impact of this procedure for the outer and inner fields. Figure 17 shows the mean relative distance modulus and its uncertainty as a function of P_{min} for both fields.

There is no statistically-significant variation in the

mean relative distance modulus of the outer field as a function of P_{min} . The primary use of the outer field Cepheids in this study is to test the maser distance of NGC 4258 against the distance to the LMC without having to worry about abundance differences (since they have the same mean metallicity). We chose $P_{min} = 6$ d as the final period cut for this sample to avoid contamination by overtone pulsators and to maximize the sample size and the overlap of period ranges between these two galaxies; note that P_{max} is 32 d for the OGLE LMC sample and 44 d for NGC 4258.

The inner field exhibits a mild trend with shorter distance moduli for smaller minimum period cut-offs, with a statistical significance of $\sim 2.7\sigma$ (P_{min} of 20 d vs. 5 d). We chose $P_{min} = 12$ d to avoid the observed bias in distance modulus at shorter periods. This value of P_{min} is similar to the typical lower limit of the Cepheid samples discovered in other galaxies observed with *HST* ($P_{min} = 10 - 15$ d).

4.2.2. Distance moduli

Taking the aforementioned period cuts into account, and using the restricted samples, we derive distance moduli *relative to the LMC* of $\Delta\mu_0 = 10.87 \pm 0.05_r \pm 0.05_s$ mag (outer field, $N = 20$ Cepheids) and $\Delta\mu_0 = 10.71 \pm 0.04_r \pm 0.05_s$ mag (inner field, $N = 69$ Cepheids).

The quoted uncertainties for these relative distance moduli arise from terms B & C of our error budget, which is listed in detail in Table 7. For comparison, we also list the error budget typical of Cepheid distance determinations based on *HST*/WFPC2 observations (e.g., Gibson et al. 2000) as well as the anticipated error budget after our follow-up NICMOS and ACS/HRC data are incorporated in the analysis and the uncertainty in the maser distance is reduced.

We derived relative distance moduli for the two fields using the methodology of Freedman et al. (2001), in which one calculates mean V and I distance moduli for the Cepheid ensemble (i.e., neglecting differential reddening among Cepheids). We did not apply rejection criteria 2+3, since they were not used by those authors, and used the same period cuts as above. We obtained $\Delta\mu_V = 11.19 \pm 0.04_r \pm 0.02_s$, $\Delta\mu_I = 11.05 \pm 0.03_r \pm 0.02_s$ and $\Delta\mu_0 = 10.86 \pm 0.04_r \pm 0.05_s$ mag ($N = 38$, outer), and $\Delta\mu_V = 11.33 \pm 0.04_r$, $\Delta\mu_I = 11.07 \pm 0.03_r$ and $\Delta\mu_0 = 10.69 \pm 0.04_r \pm 0.05_s$ mag ($N = 85$, inner). These values are consistent with a previous *HST*/WFPC2 Cepheid distance to NGC 4258 derived by Newman et al. (2001) using the same methodology. Their ALLFRAME photometry of $N = 7$ Cepheids with $P = 10 - 21$ d yielded $\Delta\mu_0 = 10.90 \pm 0.10_r \pm 0.06_s$ mag.

4.3. Metallicity dependence

The two fields under study provide an excellent opportunity to obtain a differential measurement of the metallicity dependence of the Cepheid P-L relation. We adopted an abundance gradient for NGC 4258 measured by Zaritsky et al. (1994) and expressed in their “empirical” metallicity scale as:

$$[O/H] = 8.97 \pm 0.06 - 0.49 \pm 0.08(\rho - 0.4) \text{ dex} \quad (10)$$

where ρ is the deprojected galactocentric radius, expressed as a fraction of the isophotal radius ρ_0 :

$$x = (\alpha - \alpha_0) \cos \phi + (\delta - \delta_0) \sin \phi \quad (11)$$

$$y = \{(\delta - \delta_0) \cos \phi - (\alpha - \alpha_0) \sin \phi\} / (b/a) \quad (12)$$

$$\rho = (x^2 + y^2)^{1/2} / \rho_0 \quad (13)$$

We computed the deprojected galactocentric distances of the Cepheids using these equations. We adopted $\phi = 149.75$, $b/a = 0.413$ and $\rho_0 = 7.76$ (derived from a least-squares fit to the data in Table 2 of Zaritsky et al. 1994) and a position for the center of NGC 4258 in J2000.0 coordinates of $(\alpha, \delta) = 12^{\text{h}}18^{\text{m}}57^{\text{s}}5046$, $+47^{\circ}18'14''303$ (Herrnstein et al. 2005).

Figure 18 shows the correlation between true distance modulus and deprojected galactocentric distance, or its corresponding abundance according to Eqn. 10. The sample plotted in this figure comprises all Cepheids from Table 4 with $L_V > 2$ (i.e., the restricted sample) and $P > 6$ d (outer field) or $P > 12$ d (inner field). At the suggestion of the referee, we further restricted the samples to ensure that they cover the same range of extinction, $0.05 \leq E(B-V) \leq 0.28$ mag ($N=69$ Cepheids).

A least-squares fit to the data yields $\gamma = -0.29 \pm 0.09_r \pm 0.05_s$ mag dex $^{-1}$ and $\Delta\mu_0(\text{NGC 4258-LMC}) = 10.88 \pm 0.04_r \pm 0.05_s$ mag, measured at $12 + \log[O/H] = 8.5$ dex. The best fit is represented by a solid line in Fig. 18. Since this is a differential measurement within a single galaxy, the random uncertainty arises from the scatter in the individual distance moduli and the systematic error is due to the uncertainty in the determination of the Zaritsky et al. gradient. Figure 19 shows the residuals of the individual distance moduli about the fit, plotted as a function of $E(B-V)$.

Our measurement compares favorably with the recent determination of Sakai et al. (2004), who used the tip of the red giant branch as a fiducial distance indicator under the assumption that is unaffected by abundance differences. They derived $\gamma = -0.25 \pm 0.09$ mag dex $^{-1}$ by comparing distances determined using Cepheid variables and the Tip of the Red Giant Branch (hereafter TRGB) to 17 nearby galaxies. The Cepheid distances were calculated using the same P-L relations we adopted (Eqns. 5 & 6).

Our result is also consistent with, but more statistically significant than an earlier differential determination of the metallicity effect by Kennicutt et al. (1998), who found $\gamma = -0.24 \pm 0.16$ mag dex $^{-1}$ based on *HST* observations of Cepheids in two fields within M101.

Likewise, our findings are in agreement with the values of metallicity dependence derived by Kochanek (1997) through an analysis of Cepheid magnitudes and colors in multiple galaxies, and by Sasselov et al. (1997) from a differential comparison of Large and Small Magellanic Cloud Cepheids. We find a difference in distance modulus between the inner and outer fields of $\delta\mu_0 = -0.15 \pm 0.04$ mag for a mean abundance difference of $\Delta Z = 0.45$ dex; the aforementioned studies would have predicted $\Delta\mu_0 = -0.15 \pm 0.06$ mag and -0.18 ± 0.08 mag, respectively.

Adopting the T_e metallicity scale of Kennicutt et al. (2003), the coefficient of the metallicity dependence becomes $\gamma = -0.49 \pm 0.15_r$ mag dex $^{-1}$.

4.4. A Tip of the Red Giant Branch distance to NGC 4258

At the suggestion of the referee, we determined a distance to NGC 4258 using the TRGB method (Lee et al.

1993; Sakai et al. 2004). The I -band master image of the outer field reaches a depth of $I \sim 27$ mag, which is significantly deeper than the expected TRGB magnitude. The V -band master image reaches a depth of $V \sim 28$ mag, which is sufficient to reject all stars in the I -band luminosity function with $V - I \leq 1$ mag. Such a color cut is standard practice in TRGB studies Sakai et al. (2004); Méndez et al. (2002).

The outer field I -band master object list (§2.2.2, 2), contains 2.05×10^5 objects. We rejected objects that appeared in less than half of the individual frames or exhibited signs of variability ($L_I > 0.75$), reducing the sample to 1.37×10^5 objects. Then, we rejected a small fraction (2%) of the remaining objects which exhibited a poor fit to a stellar PSF relative to other objects of the same magnitude. These are either faint galaxies or crowded stars. We matched the remaining 1.35×10^5 objects against the V -band master list and rejected all objects with $V - I < 1$ mag. Thus, the final I -band luminosity function that served as input for the TRGB detection algorithm consisted of 1.2×10^5 stars with $V - I > 1$ mag.

We computed the TRGB magnitude following the procedures described in Sakai et al. (1996) and Méndez et al. (2002). We computed a continuous luminosity function $\phi(m)$ using Equation (A1) of Sakai et al. (1996) and a logarithmic edge-detection function $E(m)$ using Equation (4) of Méndez et al. (2002). We measured the TRGB magnitude by identifying the highest peak in the product $E(m)\sqrt{\phi(m)}$ and fitting a cubic spline to the region ± 0.15 mag about the peak. Lastly, we estimated the uncertainty in our measurement of the TRGB magnitude by performing a bootstrap test with 500 simulations, as carried out by Sakai et al. (2004).

The right panel of Figure 20 shows the values of $\phi(m)$ and $E(m)$ that we obtained, resulting in a clear detection of the TRGB at $I_{TRGB} = 25.42 \pm 0.02$ mag. For reference, the TRGB magnitude is also shown as a dashed line in the I -band CMD plotted in the left panel of Figure 20; note that the actual dataset used to measure the TRGB was far more complete than what can be shown in the CMD, containing $4\times$ more stars with $V - I > 1$ mag and reaching $I \sim 27$ mag.

We corrected the observed I magnitude of the TRGB for foreground reddening (§3.2) by $A_I = 0.03$ mag. We also applied bolometric and metallicity corrections, following Equations (1)-(4) of Sakai, Zaritsky & Kennicutt (1999). These equations require the determination of the mean $V - I$ color of stars at the TRGB edge and 0.5 mag below it. We determined those values to be $(V - I)_{TRGB} = 2 \pm 0.25$ and $(V - I)_{-3.5} = 1.75 \pm 0.25$ by constructing histograms of the $V - I$ color distribution for stars within ± 0.1 mag of $I = 25.42$ and 25.92 mag, respectively. The bolometric and metallicity correction amounts to $+0.02 \pm 0.08$ mag

After these corrections, we find $I_{TRGB}^0 = 25.41 \pm 0.04_r \pm 0.08_s$ mag. The corresponding value for the LMC (Sakai, Zaritsky & Kennicutt 1999) is $I_{TRGB}^0(LMC) = 14.54 \pm 0.04_r \pm 0.06_s$ mag. Thus, we determine an LMC-relative distance modulus to NGC 4258 based on the TRGB method, of $\Delta\mu_{0,TRGB} = 10.87 \pm 0.06_r \pm 0.10_s$ mag, in excellent agreement with the Cepheid relative distance modulus obtained in §4.3. Additionally, this determination allows us to increase the sample of galaxy fields used

by Sakai et al. (2004) to determine the Cepheid metallicity dependence based on the observed difference between TRGB and Cepheid distance moduli. Figure 21 is an updated version of the bottom panel of Figure 12 of Sakai et al. (2004), with the addition of the two fields in NGC 4258. The best-fit line to the data is $\gamma = -0.27 \pm 0.06$ mag dex $^{-1}$, in very good agreement with the metallicity dependence we independently derived in §4.3.

4.5. Other Period-Luminosity relations

We considered in our analysis a second set of LMC Period-Luminosity relations derived by Sandage et al. (2004) using the sample of Udalski et al. and additional long-period Cepheids ($P = 10 - 80$ d) from the literature. These P-L relations have two slopes, with the break point set at $P = 10$ d (as motivated by Kanbur & Ngeow 2004). We found no statistically significant difference between the distance moduli derived using the Udalski et al. and the Sandage et al. relations. This is consistent with the observation of Ngeow et al. (2005) that very large samples of Cepheids ($N > 10^2$) are required to detect the change in slope of the P-L relations.

Additionally, we considered the P-L relations derived by Tammann et al. (2003) for Milky Way Cepheids. In that study, the individual distance to each variable was derived using the Baade-Wesselink method and/or the open-cluster main-sequence fitting method. The authors determined P-L relations with slopes that were significantly steeper than those derived using LMC Cepheids. They attributed the change in slope to abundance differences, since the Milky Way Cepheids in their sample have a mean metallicity that is close to solar. Recently, Saha et al. (2006) recalibrated the peak luminosities of type Ia SNe using P-L relations whose slopes vary as a function of abundance and Sandage et al. (2006) used the results to derive $H_0 = 62 \pm 6$ km s $^{-1}$ Mpc $^{-1}$.

However, there is some controversy over the P-L relation slopes that are derived via the Baade-Wesselink method. Gieren et al. (2005) applied this technique to LMC Cepheids and derived different P-L slopes than those of Udalski et al. (1999). They attributed the difference to a systematic error in the Baade-Wesselink technique, which requires the use of a period-dependent projection factor p . Gieren et al. proposed a new p factor that would resolve the discrepancy. However it still remains to be explained why Tammann et al. derived essentially identical Milky Way P-L relations using a completely independent method (open cluster main-sequence fitting). Parallax measurements to Galactic Cepheids by GAIA in the next decade may yield a definitive answer on this matter.

We can test the hypothesis of Saha et al. (2006) with our large sample of Cepheids in the inner field, since the application of the correct V and I P-L relations should lead to a distribution of distance moduli that is uncorrelated with period. We started with the restricted sample of 195 Cepheids in the inner field and excluded 23 objects with anomalous amplitude ratios (§3.3.1), 24 variables with $P < 6$ d, and 5 objects with μ_W outside 11 ± 1 mag. Next, we fit a slope to $\Delta\mu_0$ vs P using an iterative least-absolute-deviation procedure with 3σ clipping, which rejected 6 outliers. Thus, our final sample consisted of 137 Cepheids. We carried out this exercise for three choices of

P-L relation: Udalski et al. (1999), Sandage et al. (2004), and Tammann et al. (2003). We tested the null hypothesis by computing the Spearman rank-order correlation coefficient r_s for each choice of P-L relation. For comparison, we carried out the same exercise for the outer field sample and the P-L relations of Udalski et al. Figure 22 shows the result of these tests.

The LMC P-L relations are a good fit to the samples of both fields. There is a small correlation for the inner field with $r_s = 0.2$ (2.5σ), which decreases to $r_s = 0.15$ (1.3σ) if we use $P_{min} = 12$ d as in §4.2. The application of the Milky-Way P-L relations of Tammann et al. (2003) to the inner field sample yields a distribution that deviates noticeably from the null hypothesis, with $r_s = 0.6$ (6.8σ). The correlation is still present, with $r_s = 0.45$ (4σ), for $P_{min} = 12$ d. Thus, we conclude that the LMC P-L relations are a better fit to both samples, regardless of their abundance difference.

4.6. Implications for H_0 and w

Since the mean abundance of LMC Cepheids ($12 + \log[O/H] = 8.5$ dex) lies within the range spanned by our sample of variables (Fig. 18) we have measured $\Delta\mu_0(\text{NGC 4258-LMC}) = 10.88 \pm 0.04_r \pm 0.05_s$ mag (§4.3). Combined with the maser distance modulus to NGC 4258, we infer the distance modulus of the LMC to be $\mu_0(LMC) = 18.41 \pm 0.10_r \pm 0.13_s$ mag. This corresponds to a distance of $D(LMC) = 48.1 \pm 2.3_r \pm 2.9_s$ kpc, which is in excellent agreement with the value of 48.3 ± 1.4 kpc derived from eclipsing binaries (see Case II in Table 8 of Fitzpatrick et al. 2003). Importantly, both distance estimates are mainly geometric, independent of each other, and do not rely on any “standard candles”.

We note that in the near future, there will be four galaxies with “geometric distances” that can serve as absolute calibrators for the Cepheid Distance Scale: the Large Magellanic Cloud (with multiple DEB distances, see Fitzpatrick et al. 2003, and references therein), Messier 31 (with a DEB distance by Ribas et al. 2005), Messier 33 (with a DEB distance by Bonanos et al. 2006) and NGC 4258 (with the maser distance by Humphreys et al., in prep.). Thus, we can expect a significant reduction in the uncertainty of the “first rung” of the Extragalactic Distance Scale, which has been a dominant source of uncertainty in recent determinations of H_0 .

The implied decrease in the distance to the LMC derived in this paper, relative to the adopted value of $D = 50.1 \pm 2.3$ kpc (Freedman et al. 2001; Saha et al. 2001), affects previously-derived values of H_0 by $\sim +3\%$. The increase in the coefficient of the metallicity dependence from $\gamma = -0.2 \pm 0.2$ mag dex $^{-1}$ (adopted by Freedman et al. 2001) to $-0.29 \pm 0.09_r \pm 0.05_s$ mag dex $^{-1}$ (§4.3) has an opposite effect on H_0 of $\sim -2\%$. As a result, the net effect on the calibration of secondary distance indicators is mitigated. Table 8 shows a re-calculation of the peak absolute V magnitude of type Ia SNe recently determined by Riess et al. (2005), which changes only by -0.03 mag to $M_V^0 = -19.14 \pm 0.06$ mag. The resulting value of H_0 is $74 \pm 3_r \pm 6_s$ km s $^{-1}$ Mpc $^{-1}$.

Recently, Spergel et al. (2006) presented a determination of cosmological parameters based on 3 years of WMAP observations. CMB observations cannot provide strong constraints on the value of H_0 on their own, due to

degeneracies in parameter space (Tegmark et al. 2004). Figure 23 shows the degeneracy in the $\Omega_M - w$ plane. The addition of an independent of H_0 from Cepheids significantly reduces that degeneracy (Hu 2005).

We calculated the improvement due to a prior on H_0 (solid contours of Fig. 23) by resampling the Monte Carlo Markov Chains kindly made available by the WMAP team, using Eq. B4 of Lewis & Bridle (2002). We also calculated marginalized probability distributions for w for increasingly more accurate priors on H_0 . The results, which are shown in Figure 24, indicate that a 5% prior on H_0 would reduce the 1σ uncertainty in w to ± 0.1 . As shown by Spergel et al., the combination of CMB data with more than one prior (e.g., Cepheids, type Ia SNe and large-scale structure) can further refine the measurement of w .

A determination of H_0 to 5% (see Table 7) is a conservative goal for the near term. It will require the re-estimation of a maser distance to NGC 4258 (Humphreys et al., in prep.), the analysis of follow-up observations of the Cepheids discovered in this paper with other *HST* instruments (Bersier et al., in prep.; Macri et al., in prep.), and the inclusion in the Cepheid sample of longer-period ($40 \text{ d} < P < 90 \text{ d}$) variables discovered with GMOS on Gemini North (Macri & Smith, in prep.).

Further improvement on the accuracy of H_0 , down to 1%, may be obtained through maser distances to a large number of galaxies in the Hubble flow, which could be discovered with the Square Kilometer Array and its prototypes (Greenhill 2004).

5. CONCLUSIONS

The five main results presented in this paper are the following:

1. We discovered 281 Cepheid variables in two fields located within the galaxy NGC 4258, with accurately calibrated *BVI* photometry in twelve epochs per band.
2. We determined a relative distance modulus between NGC 4258 and the Large Magellanic Cloud, based on Cepheid variables, of $\Delta\mu_0 = 10.88 \pm 0.04_r \pm 0.05_s$ mag.
3. We determined a relative distance modulus between these two galaxies, based on the Tip of the Red Giant Branch method, of $\Delta\mu_{0,TRGB} = 10.87 \pm 0.04_r$ mag.
4. We measured a metallicity dependence of the Cepheid distance scale of $\gamma = -0.29 \pm 0.09_r \pm 0.05_s$ mag dex $^{-1}$.
5. Our observations are best fit with P-L relations that do not invoke changes in slope as a function of abundance.

We thank the Telescope Allocation Committee of the *Hubble Space Telescope* for granting telescope time for this project in Cycle 12. We were partially supported by HST Grant HST-GO-09810, provided by NASA through a grant from the Space Telescope Science Institute, which is operated by the Association of Universities for Research in Astronomy, Incorporated, under NASA contract NAS5-26555. Support for L.M.M. was provided by NASA through Hubble Fellowship grant HST-HF-01153 from the Space Telescope Science Institute and by the National Science Foundation through a Goldberg Fellowship from the National Optical Astronomy Observatory.

Some of the data presented in this paper were obtained from the Multimission Archive at the Space Telescope Science Institute (MAST). We acknowledge the use of

the Canadian Astronomy Data Centre, which is operated by the Herzberg Institute of Astrophysics, National Research Council of Canada. This research has made use of the NASA/IPAC Extragalactic Database (NED) which is operated by the Jet Propulsion Laboratory, California Institute of Technology, under contract with the National Aeronautics and Space Administration. We acknowledge the use of the Legacy Archive for Microwave Background Data Analysis (LAMBDA), which is supported by the NASA Office of Space Science. We thank

the WMAP team for making their data publicly available. This research has made use of NASA's Astrophysics Data System Bibliographic Services.

L.M.M. wishes to thank Arjun Dey, Shashi Kanbur, Chris Kochanek, Tom Matheson, Jeremy Mould, Adam Riess, Abi Saha, Peter Stetson and Matías Zaldarriaga for helpful discussions and comments during the preparation of this paper. We thank the referee, Shoko Sakai, for her helpful comments and suggestions during the review of this manuscript.

REFERENCES

- Benedict, G. F., et al. 2002, *AJ*, 124, 1695
 Bersier, D., et al., in preparation
 Bonanos, A. Z., et al. 2006, *ApJ*, in press
 Cardelli, J. A., Clayton, G. C., & Mathis, J. S. 1989, *ApJ*, 345, 245
 de Vaucouleurs, G., et al. 1991, *Third Reference Catalogue of Bright Galaxies* (New York: Springer-Verlag)
 Eisenstein, D., & White, M. 2004, *Phys. Rev. D*, 70, 103523
 Fiorentino, G., et al. 2002, *ApJ*, 576, 402
 Fitzpatrick, E. L., et al. 2003, *ApJ*, 587, 685
 Ford, H. C., et al. 2003, in *SPIE Proc.: Future EUV/UV and Visible Space Astrophysics Missions and Instrumentation.*, ed. J. C. Blades & O. H. W. Siegmund, Vol. 4854, 81–94
 Freedman, W. L., et al. 2001, *ApJ*, 553, 47
 Gibson, B. K., et al. 2000, *ApJ*, 529, 723
 Gieren, W., et al. 2005, *ApJ*, 627, 224
 Greenhill, L. J., et al. 1995, *ApJ*, 440, 619
 Greenhill, L. J. 2004, *New Astronomy Review*, 48, 1079
 Herrnstein, J. R., et al. 1999, *Nature*, 400, 539
 Herrnstein, J. R., et al. 2005, *ApJ*, 629, 719
 Hu, W. 2005, in *ASP Conf. Ser. 339: Observing Dark Energy*, ed. S. C. Wolf & T. R. Lauer, 215–234
 Humphreys, E. M. L., et al., 2005a, in *ASP Conf. Ser. 340: Future Directions in High Resolution Astronomy*, ed. J. Romney & M. Reid
 Humphreys, E. M. L., et al., 2005b, *Ap&SS*, 295, 285
 Humphreys, E. M. L., et al., in preparation
 Kaluzny, J., et al. 1998, *AJ*, 115, 1016
 Kanbur, S. M., & Ngeow, C. 2004, *MNRAS*, 350, 962
 Kennicutt, R. C., et al. 1998, *ApJ*, 498, 181
 Kennicutt, R. C., Bresolin, F., & Garnett, D. 2003, *ApJ*, 591, 801
 Kochanek, C. S. 1997, *ApJ*, 491, 13
 Lafler, J., & Kinman, T. D. 1965, *ApJS*, 11, 216
 Lee, M. G., Freedman, W. L., & Madore, B. F. 1993, *ApJ*, 417, 553
 Leonard, D. C., et al. 2003, *ApJ*, 594, 247
 Lewis, A., & Bridle, S. 2002, *Phys. Rev. D*, 66, 103511
 Macri, L. M., & Smith, C. E., in preparation
 Macri, L. M., et al., in preparation
 Madore, B. F., & Freedman, W. L. 2005, *ApJ*, 630, 1054
 Méndez, B., et al. 2002, *AJ*, 124, 213
 Mink, D. J. 2002, in *ASP Conf. Ser. 281: ADASS XI*, ed. D. A. Bohlender, D. Durand, & T. H. Handley, 169
 Miyoshi, M., et al. 1995, *Nature*, 373, 127
 Mochejska, B. J., et al. 2000, *AJ*, 120, 810
 Newman, J. A., et al. 2001, *ApJ*, 553, 562
 Ngeow, C.-C., et al. 2005, *MNRAS*, 363, 831
 Nikolaev, S., et al. 2004, *ApJ*, 601, 260
 Pavlovsky, C., et al. 2005, *The ACS Data Handbook, Version 4.0* (Baltimore:STScI)
 Riess, A., & Mack, J. 2004, *ACS ISR 04-06* (Baltimore:STScI)
 Riess, A. G., et al. 2005, *ApJ*, 627, 579
 Saha, A., & Hoessel, J. G. 1990, *AJ*, 99, 97
 Saha, A., et al. 1996, *ApJ*, 466, 55
 Saha, A., et al. 2001, *ApJ*, 562, 314
 Saha, A., et al. 2006, *ApJS*, 165, 108
 Sakai, S., et al. 1996, *ApJ*, 461, 713
 Sakai, S., et al. 1999, *AJ*, 119, 1197
 Sakai, S., et al. 2004, *ApJ*, 608, 42
 Sandage, A., & Tammann, G. A. 1987, *A revised Shapley-Ames catalog of bright galaxies* (Washington, D.C.: Carnegie Institution of Washington)
 Sandage, A. 1988, *PASP*, 100, 935
 Sandage, A., Tammann, G. A., & Reindl, B. 2004, *A&A*, 424, 43
 Sandage, A., et al. 2006, *ApJ*, in press
 Sasselov, D. D., et al. 1997, *A&A*, 324, 471
 Schlegel, D. J., Finkbeiner, D. P., & Davis, M. 1998, *ApJ*, 500, 525
 Sirianni, M., et al. 2003, *ApJS*, 148, 175
 Spergel, D. N., et al. 2006, *ApJ*, in press
 Stetson, P. B. 1987, *PASP*, 99, 191
 —. 1990, *PASP*, 102, 932
 —. 1994, *PASP*, 106, 250
 —. 1996, *PASP*, 108, 851
 Stetson, P. B., & Gibson, B. K. 2001, *MNRAS*, 328, L1
 Stetson, P. B., et al. 1998, *ApJ*, 508, 491
 Ribas, I., et al. 2005, *ApJ*, 635, 37
 Tammann, G. A., Sandage, A., & Reindl, B. 2003, *A&A*, 404, 423
 Tegmark, M., et al. 2004, *Phys. Rev. D*, 69, 103501
 Tully, R. B., & Fisher, J. R. 1987, *Nearby galaxies Atlas* (Cambridge: Cambridge University Press)
 Udalski, A., et al. 1999, *Acta Astronomica*, 49, 223
 van der Marel, R. P. 2001, *AJ*, 122, 1827
 Zaritsky, D., Kennicutt, R. C., & Huchra, J. P. 1994, *ApJ*, 420, 87

Due to size limitations imposed by arxiv.org, print-quality Figures appear only in the full-resolution PDF and PS versions, which are available at <http://www.noao.edu/staff/lmacri/0608211-full.pdf> or <http://www.noao.edu/staff/lmacri/0608211-full.ps.gz>, respectively.

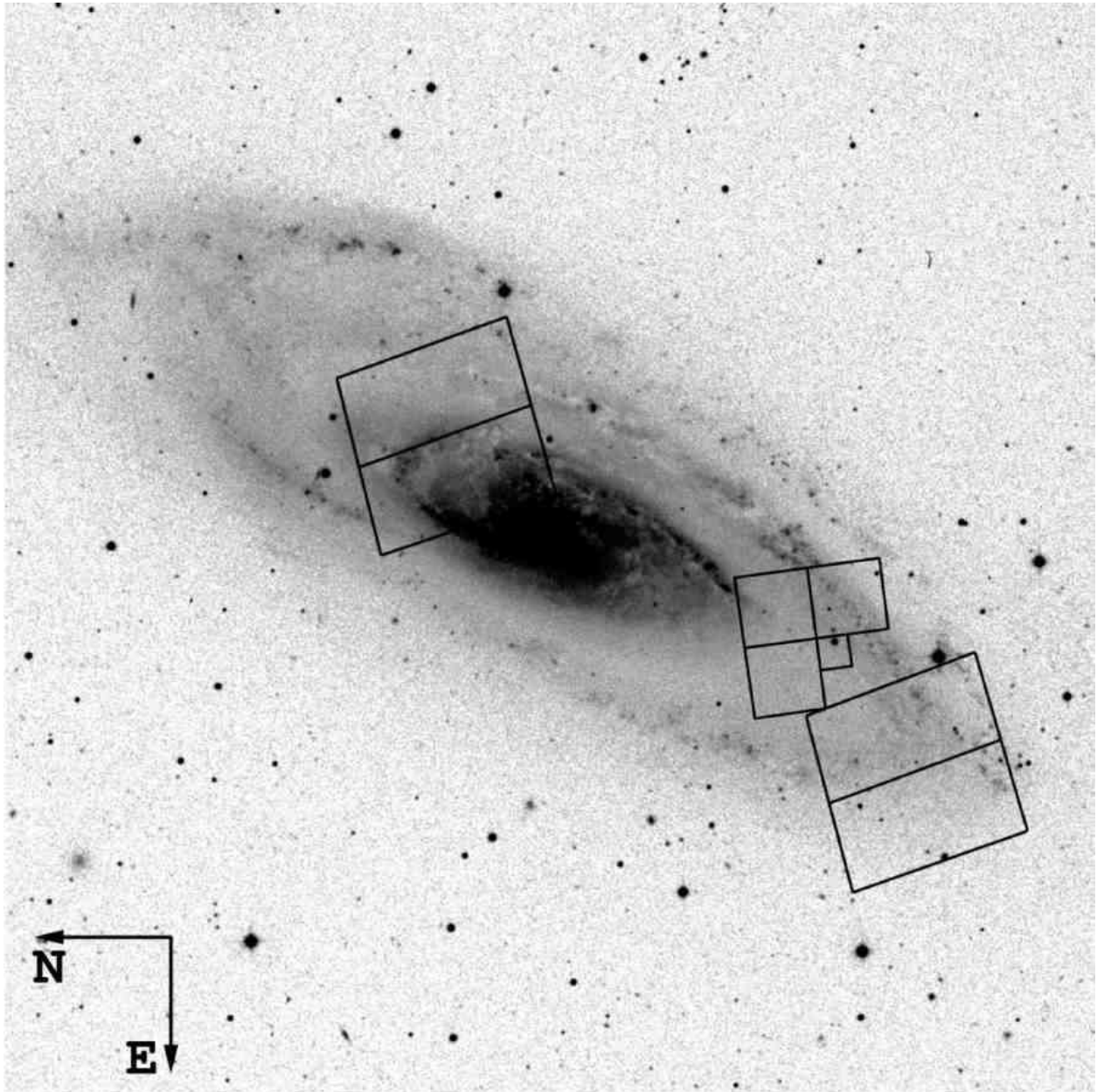


FIG. 1.— A blue DPOSS image of NGC 4258 showing the two ACS/WFC fields observed for this project and the WFPC2 field previously studied by Newman et al. (2001).

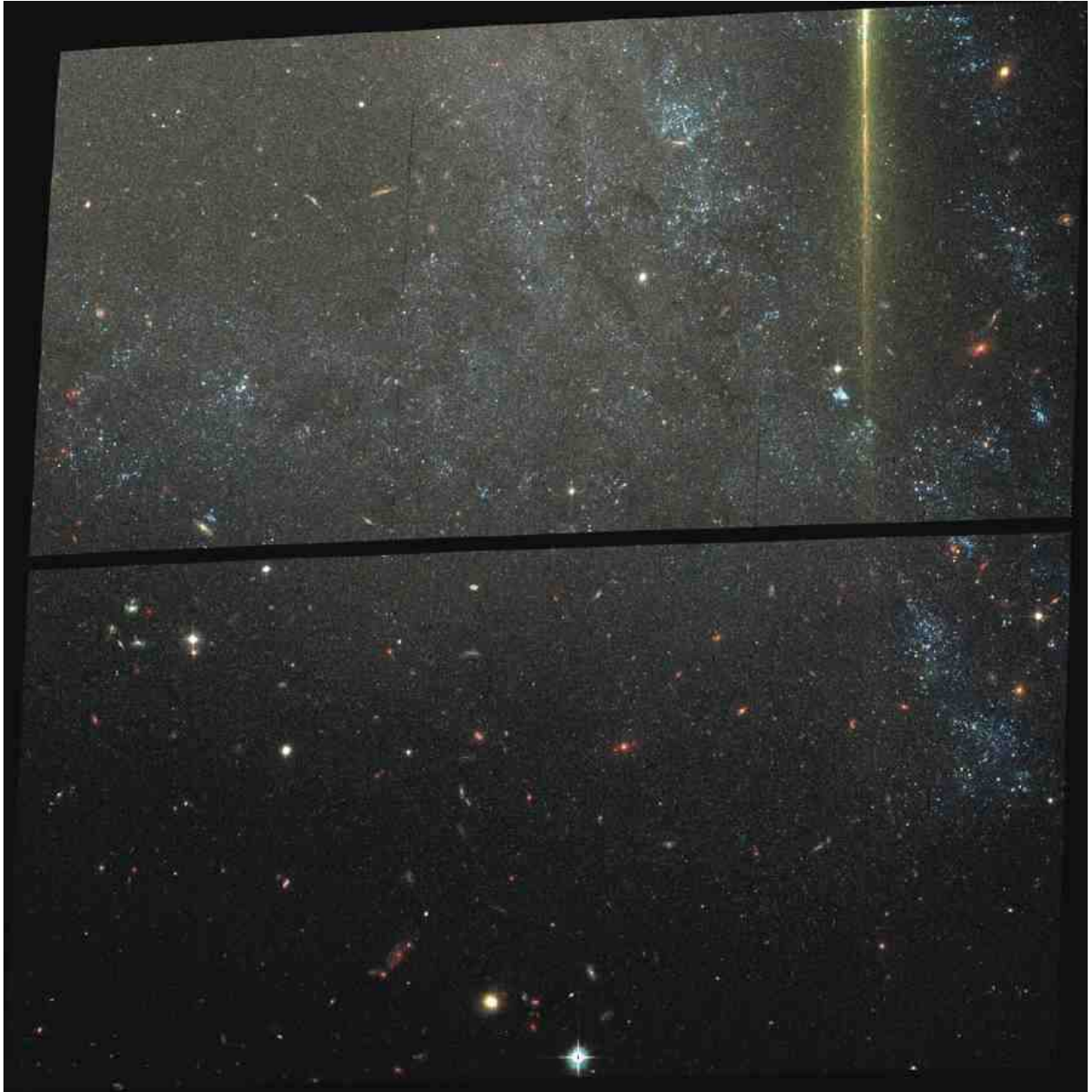


FIG. 2.— A color composite of the *HST* ACS/WFC outer field of NGC 4258.

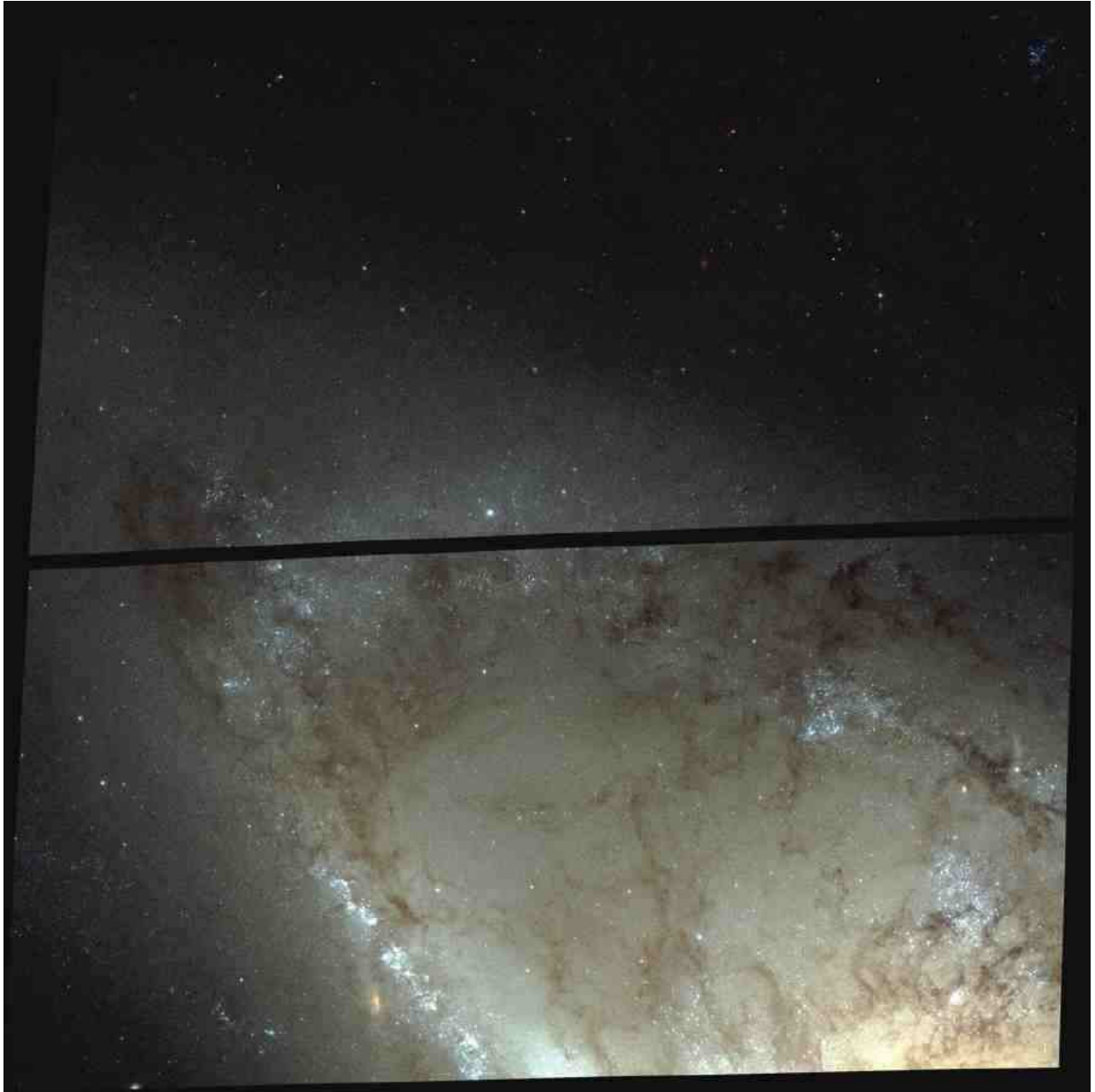


FIG. 3.— A color composite of the *HST* ACS/WFC inner field of NGC 4258.

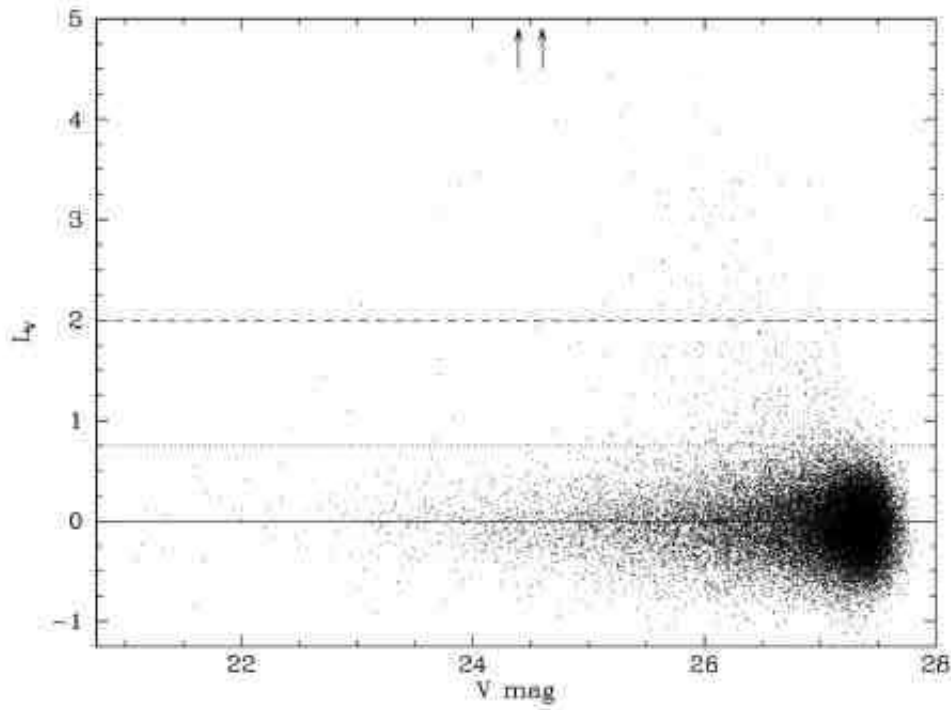


FIG. 4.— Distribution of the modified Welch-Stetson variability index L_V (Stetson 1996) as a function of V magnitude for objects in the outer field, after sigma-scaling. The dotted and dashed lines represent the minimum values of L_V for the extended and restricted samples, respectively. Two variables with $L_V > 6$ are represented by arrows.

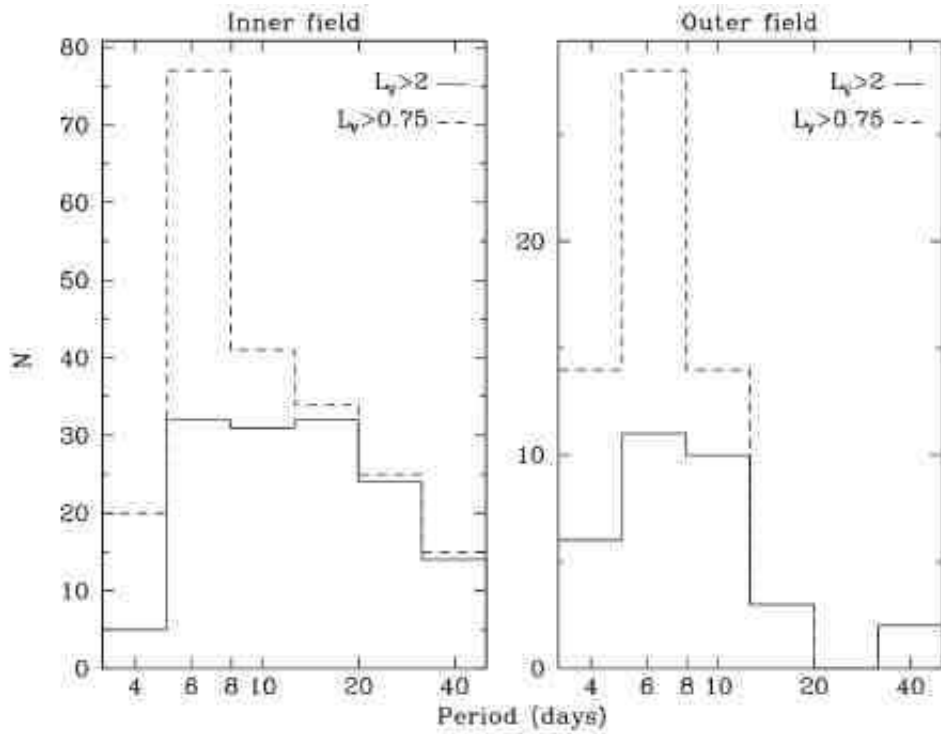


FIG. 5.— Period histograms for the final Cepheid samples after application of the selection criteria listed in §3.3. Left panel: Inner field. Right panel: Outer field. Dashed line: extended sample. Solid line: restricted sample.

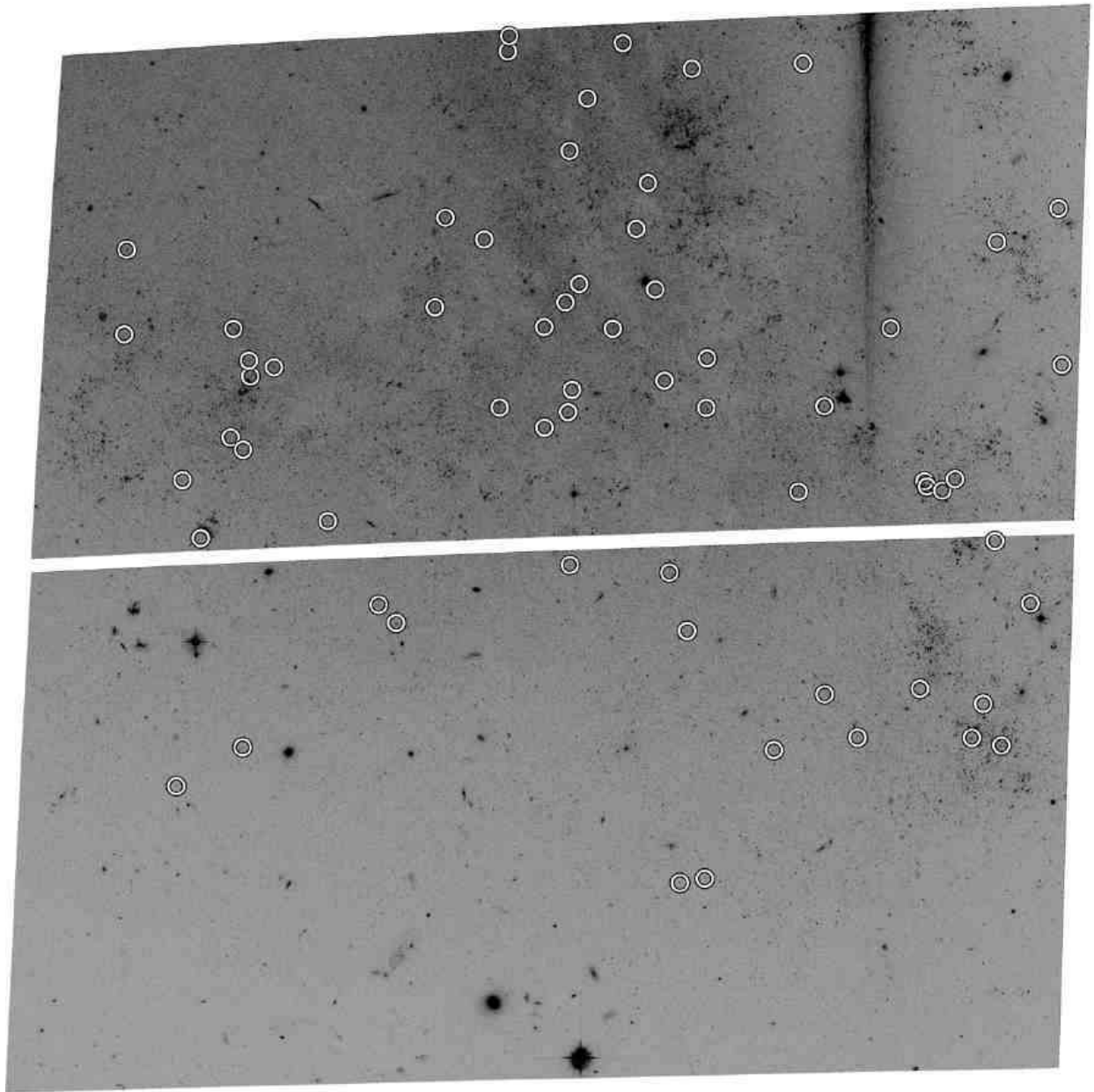


FIG. 6.— Master V-band image of the ACS outer field. The location of the Cepheids listed in Table 4 are marked with open circles.

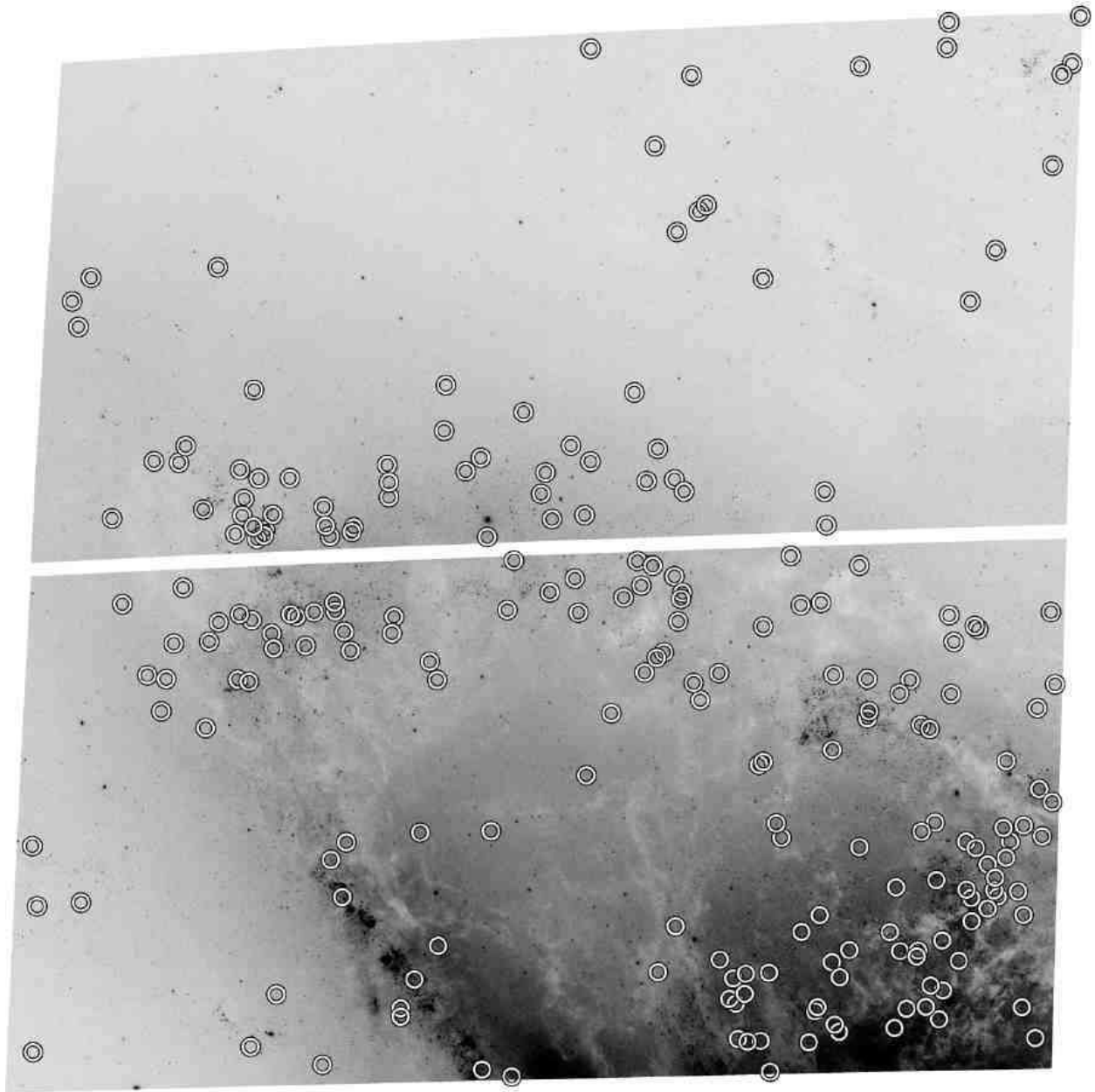


FIG. 7.— Master V-band image of the ACS inner field. The location of the Cepheids listed in Table 4 are marked with open circles.

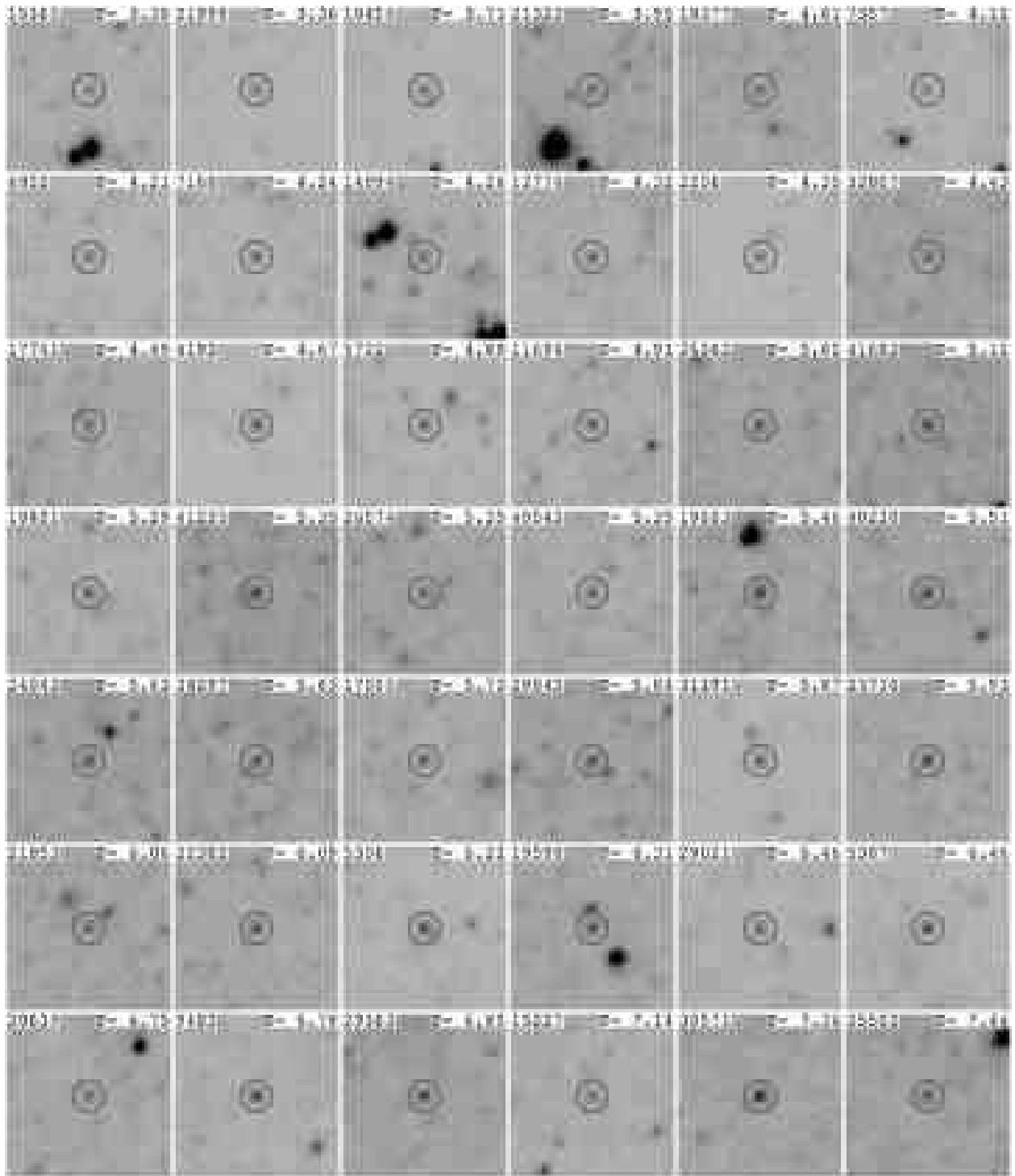
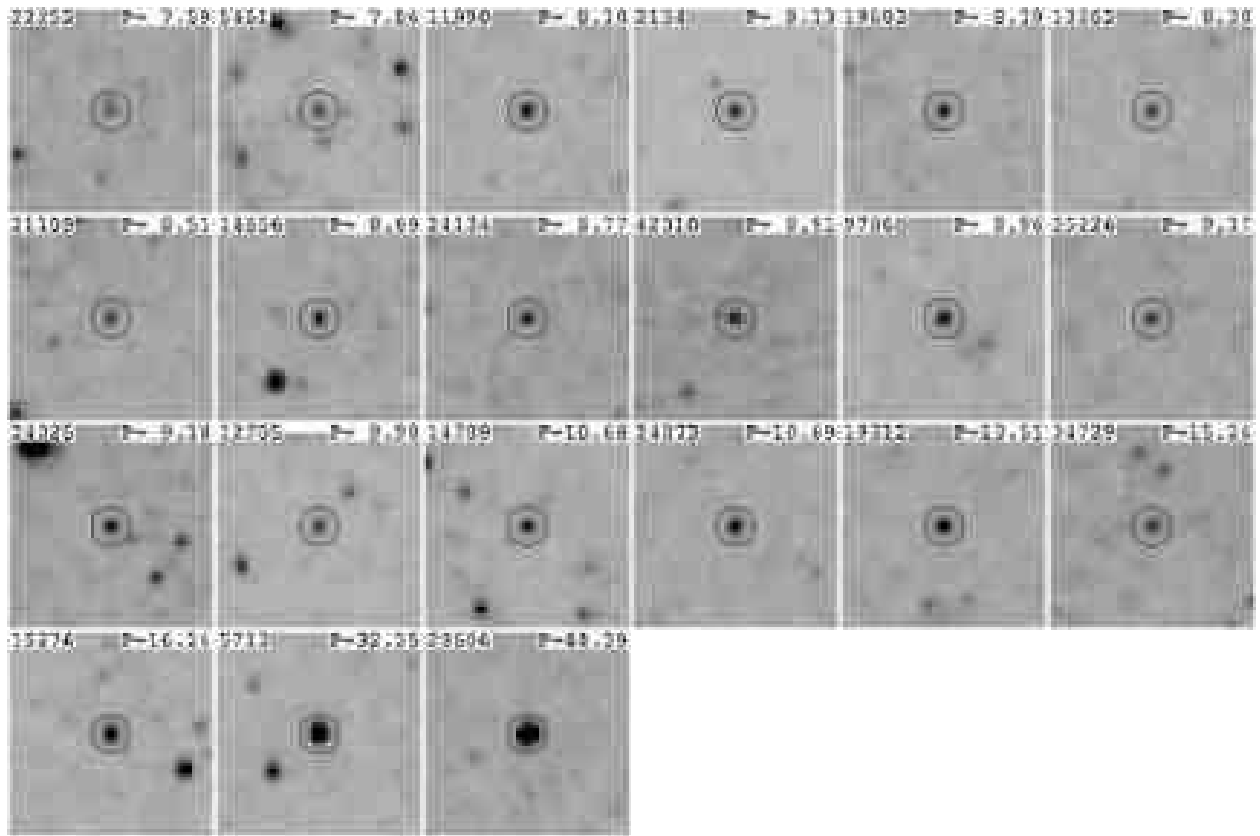


FIG. 8A.— Individual finding charts for the Cepheids listed in Table 4. Each box is $2.5''$ on a side.



Inner field:

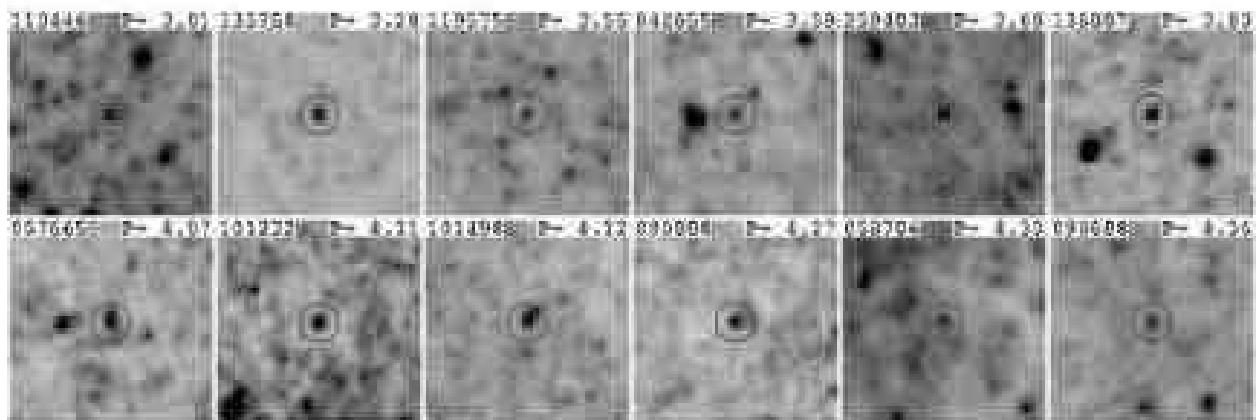


FIG. 8B.— Individual finding charts for the Cepheids listed in Table 4. Each box is 2.5'' on a side.

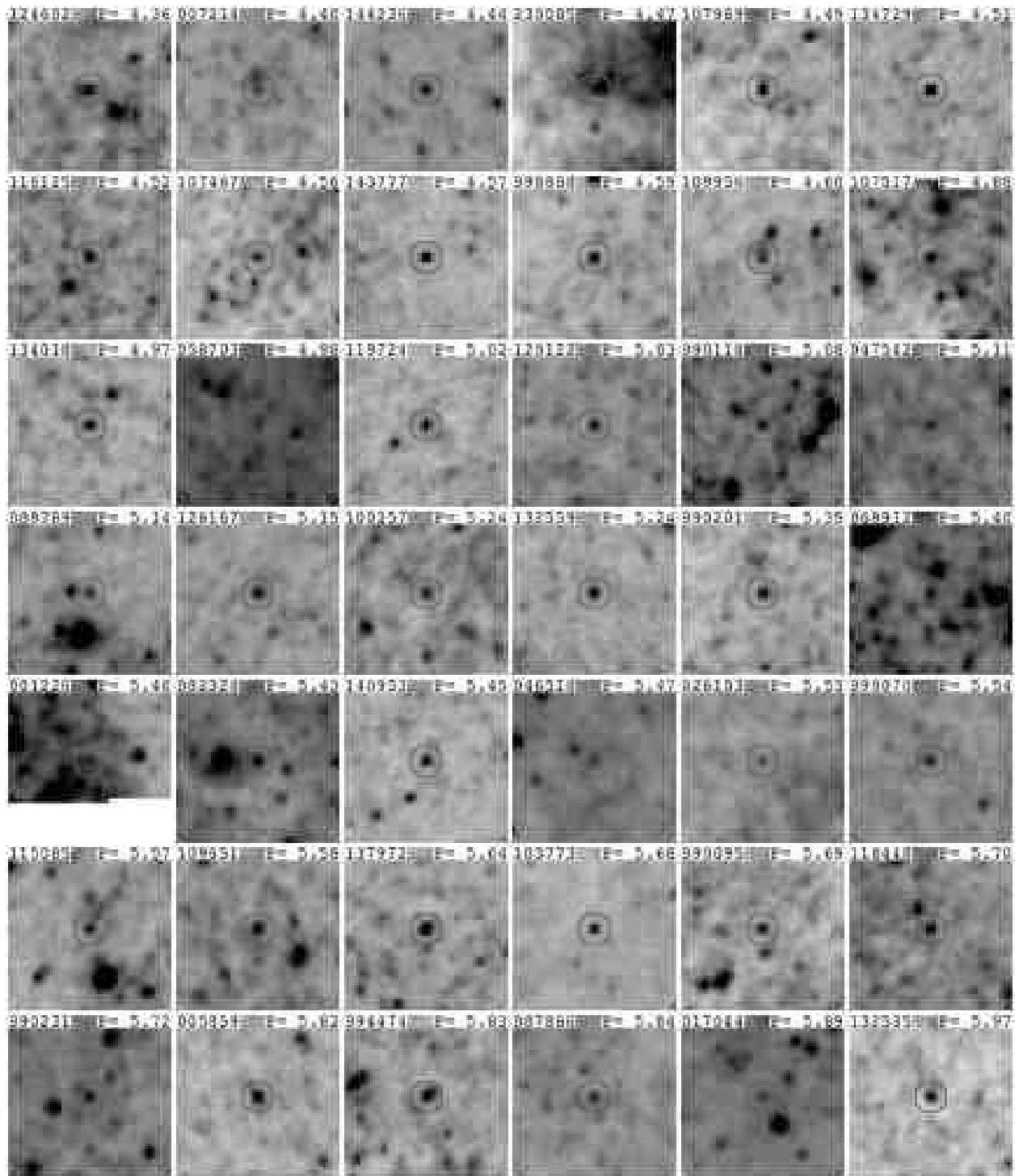


FIG. 8C.— Individual finding charts for the Cepheids listed in Table 4. Each box is $2.5''$ on a side.

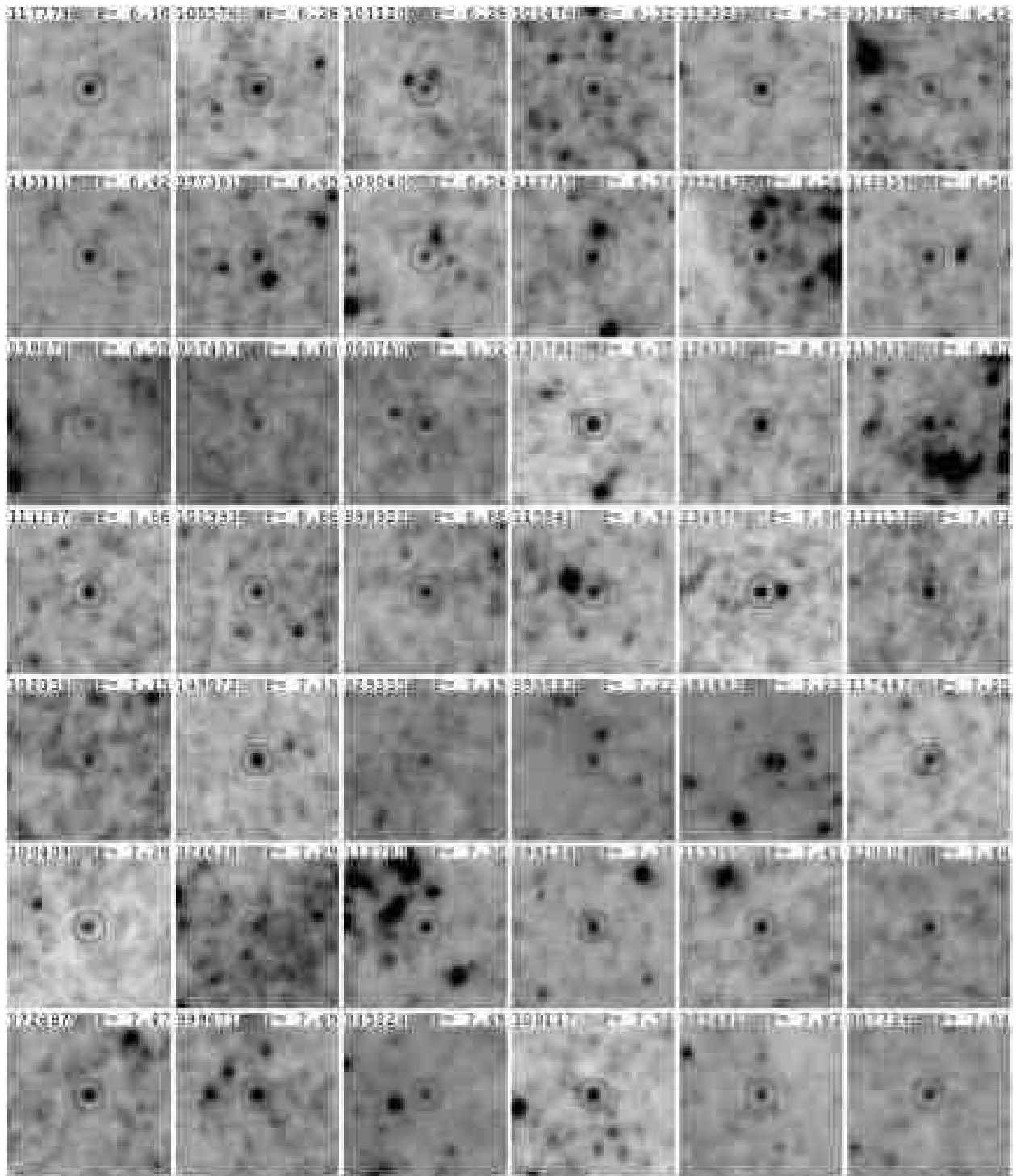


FIG. 8D.— Individual finding charts for the Cepheids listed in Table 4. Each box is $2.5''$ on a side.

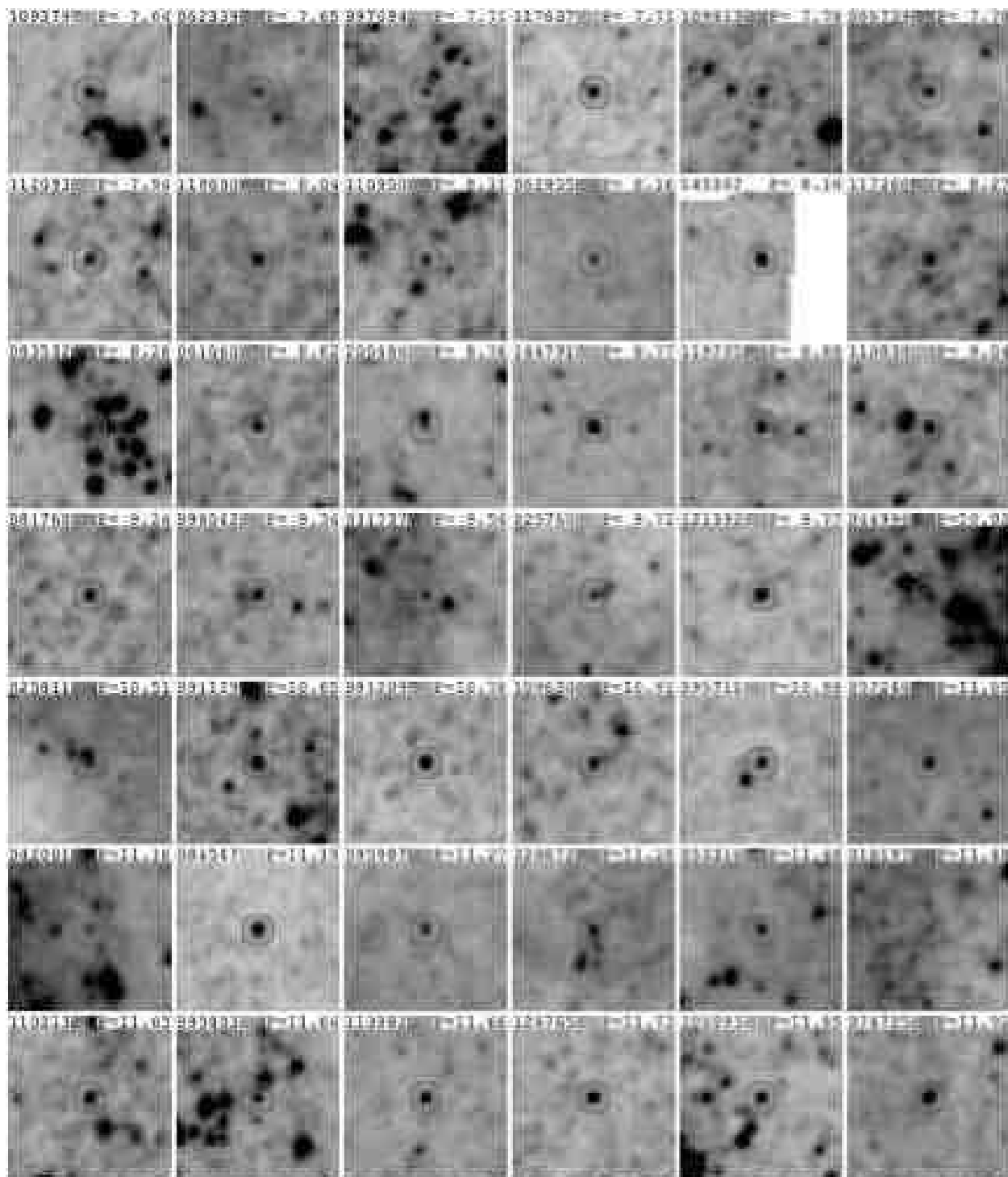


FIG. 8E.— Individual finding charts for the Cepheids listed in Table 4. Each box is $2.5''$ on a side.

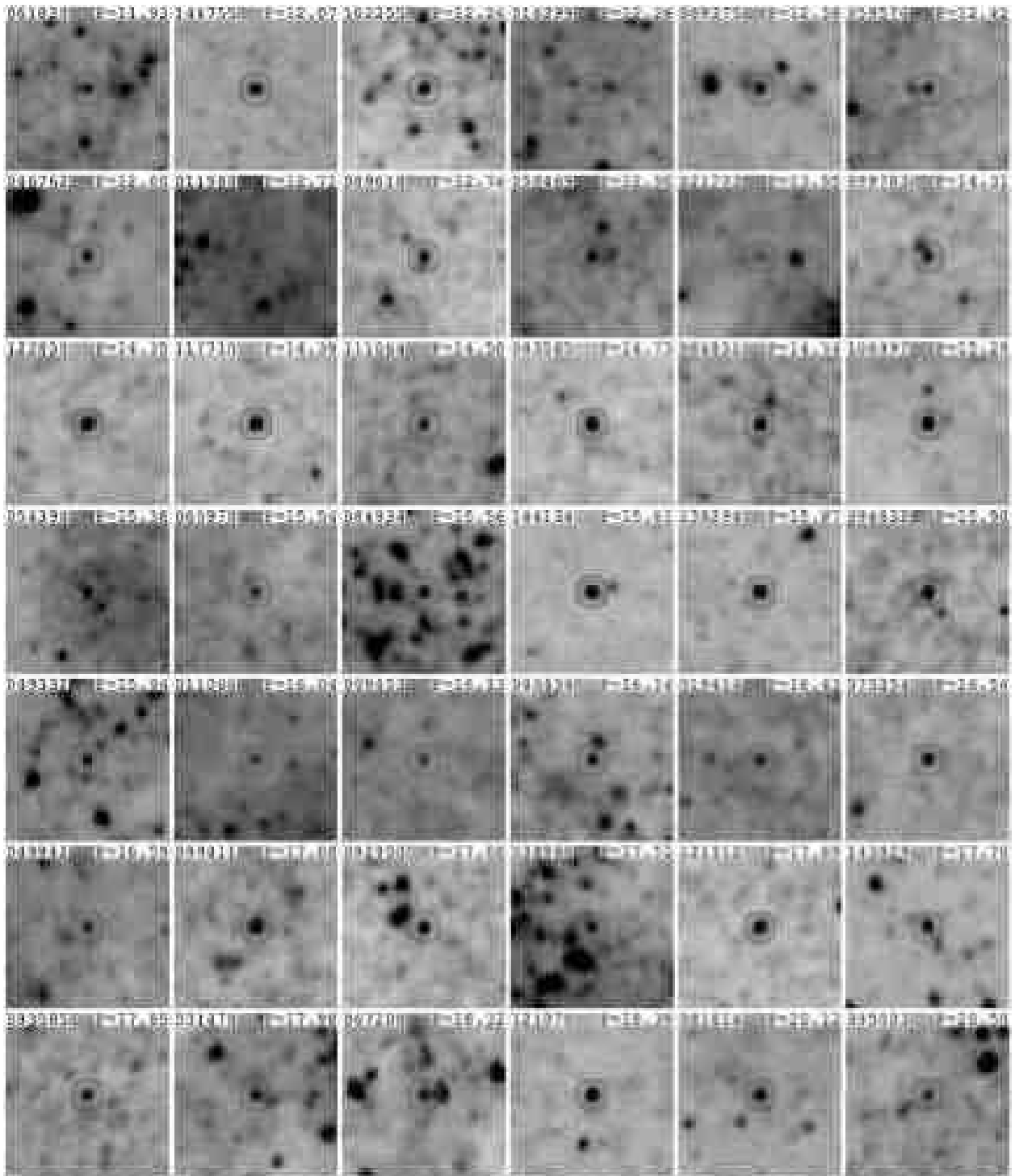


FIG. 8F.— Individual finding charts for the Cepheids listed in Table 4. Each box is $2.5''$ on a side.

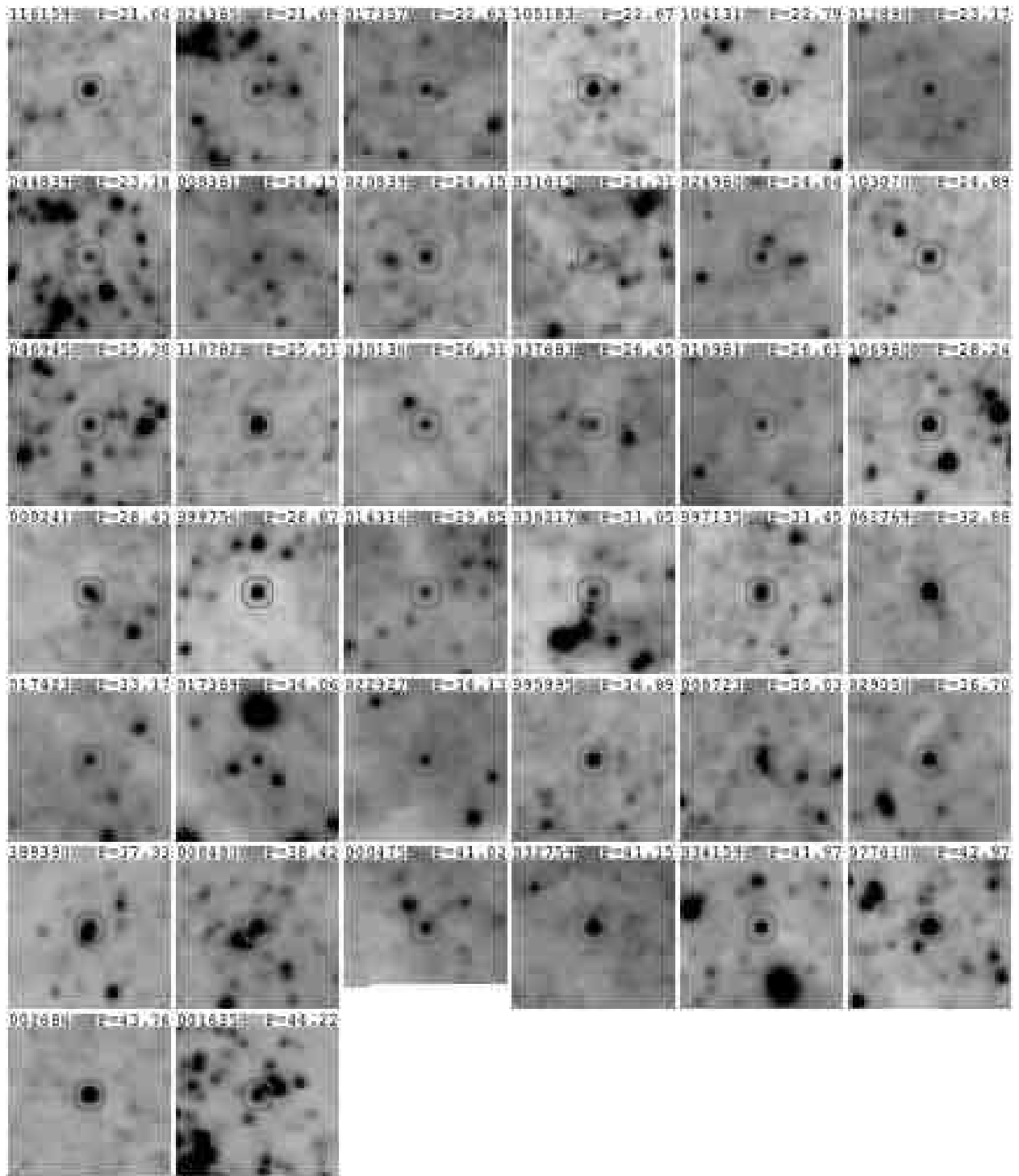


FIG. 8C.— Individual finding charts for the Cepheids listed in Table 4. Each box is $2.5''$ on a side.

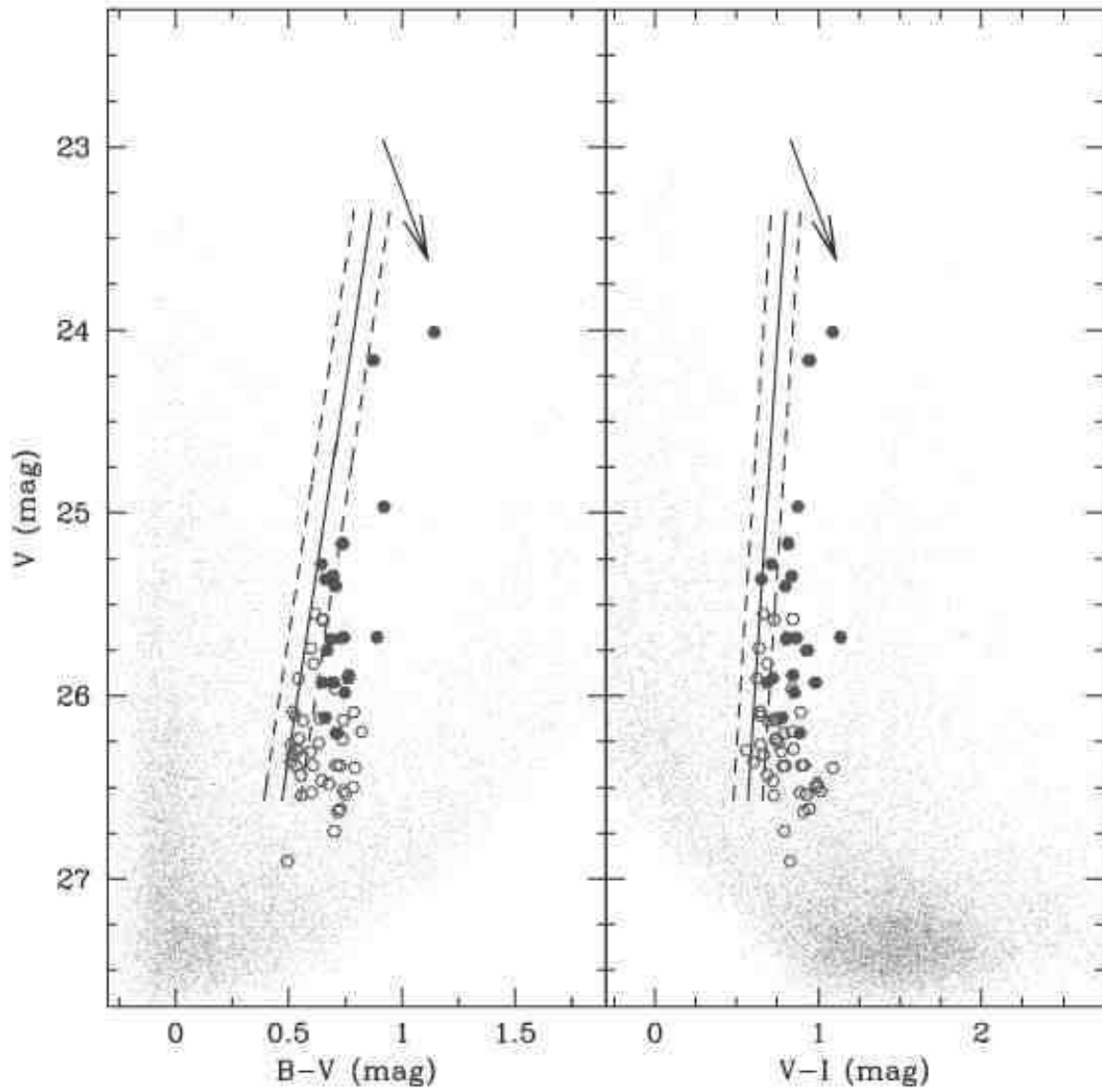


FIG. 9.— Color-magnitude diagrams for objects in the outer field of NGC 4258. Cepheids are plotted using filled and open symbols for the restricted and extended samples, respectively. Field stars are represented by small dots. The dashed lines represent the zero-reddening instability strip of LMC Cepheids and its 2σ width. The arrows indicate the effect of $E(B-V) = 0.2$ mag.

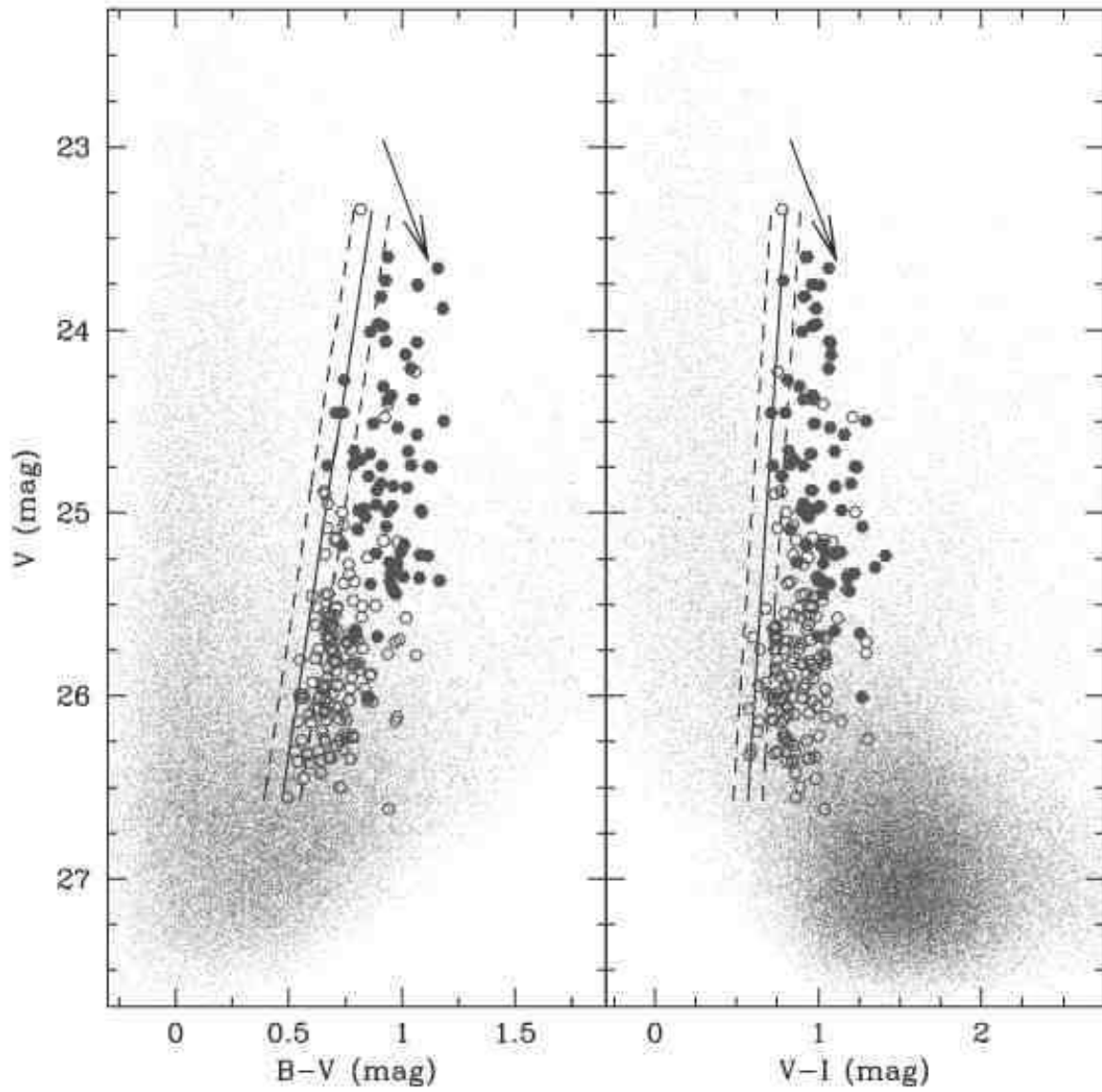


FIG. 10.— Color-magnitude diagrams for objects in the inner field of NGC 4258. Cepheids are plotted using filled and open circles for the restricted and extended samples, respectively. Field stars are represented by small dots. The dashed lines represent the zero-reddening instability strip of LMC Cepheids and its 2σ width. The arrows indicate the effect of $E(B-V) = 0.2$ mag.

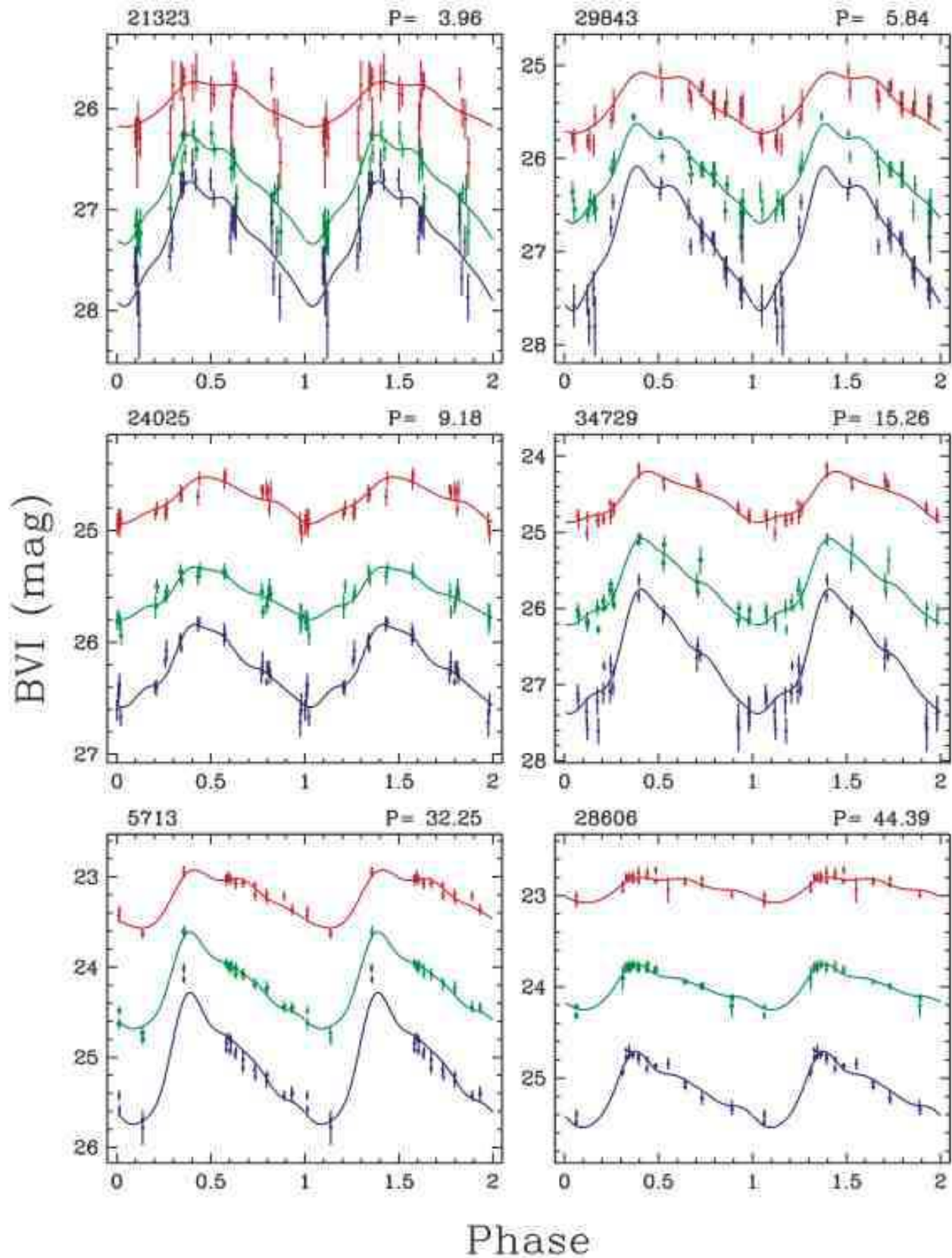


FIG. 11.— Representative light curves of Cepheids in the outer field. Blue: *B*; green: *V*; red: *I*. The solid lines indicate the best-fit light curve template from Stetson (1996).

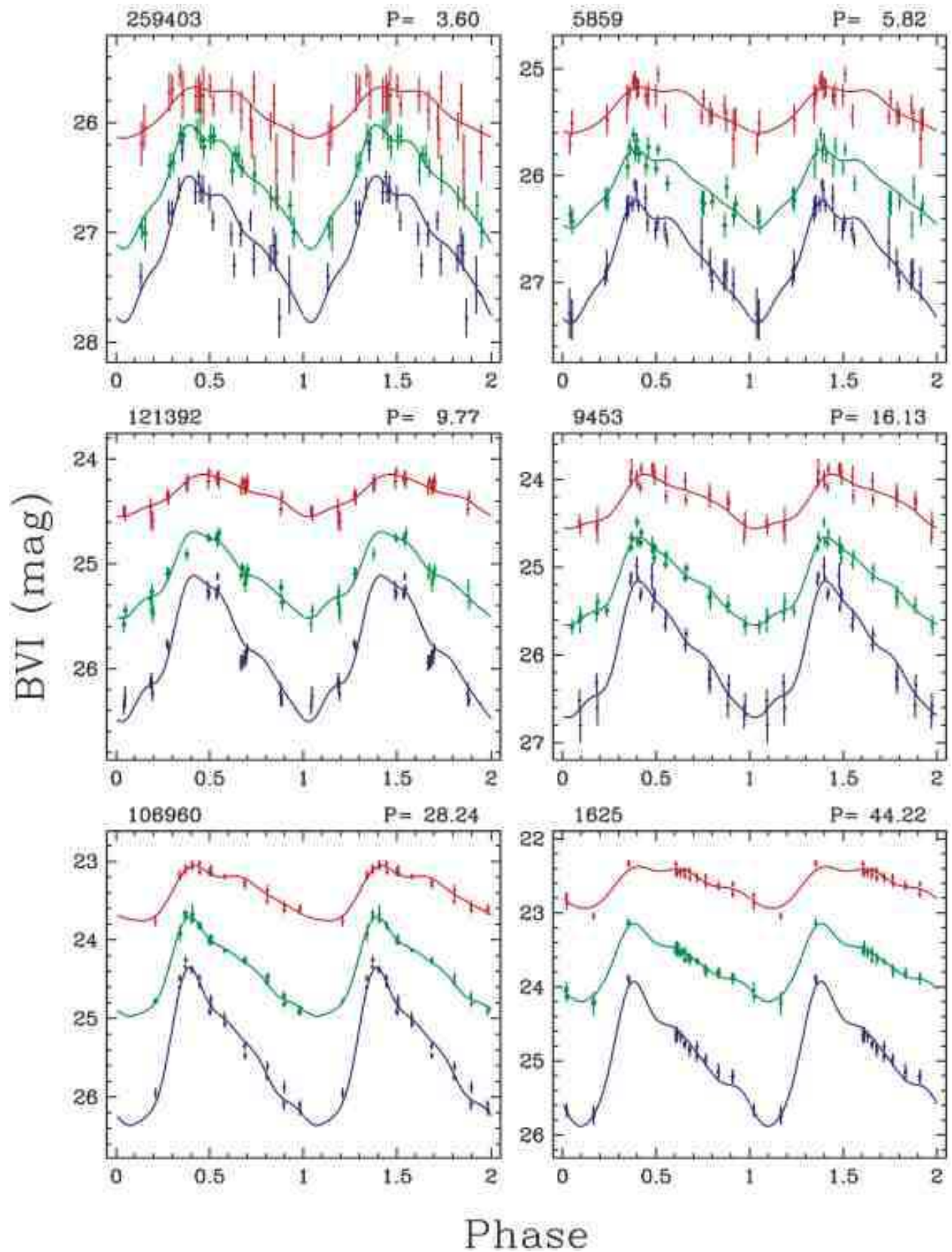


FIG. 12.— Representative light curves of Cepheids in the inner field. Blue: B ; green: V ; red: I . The solid lines indicate the best-fit light curve template from Stetson (1996).

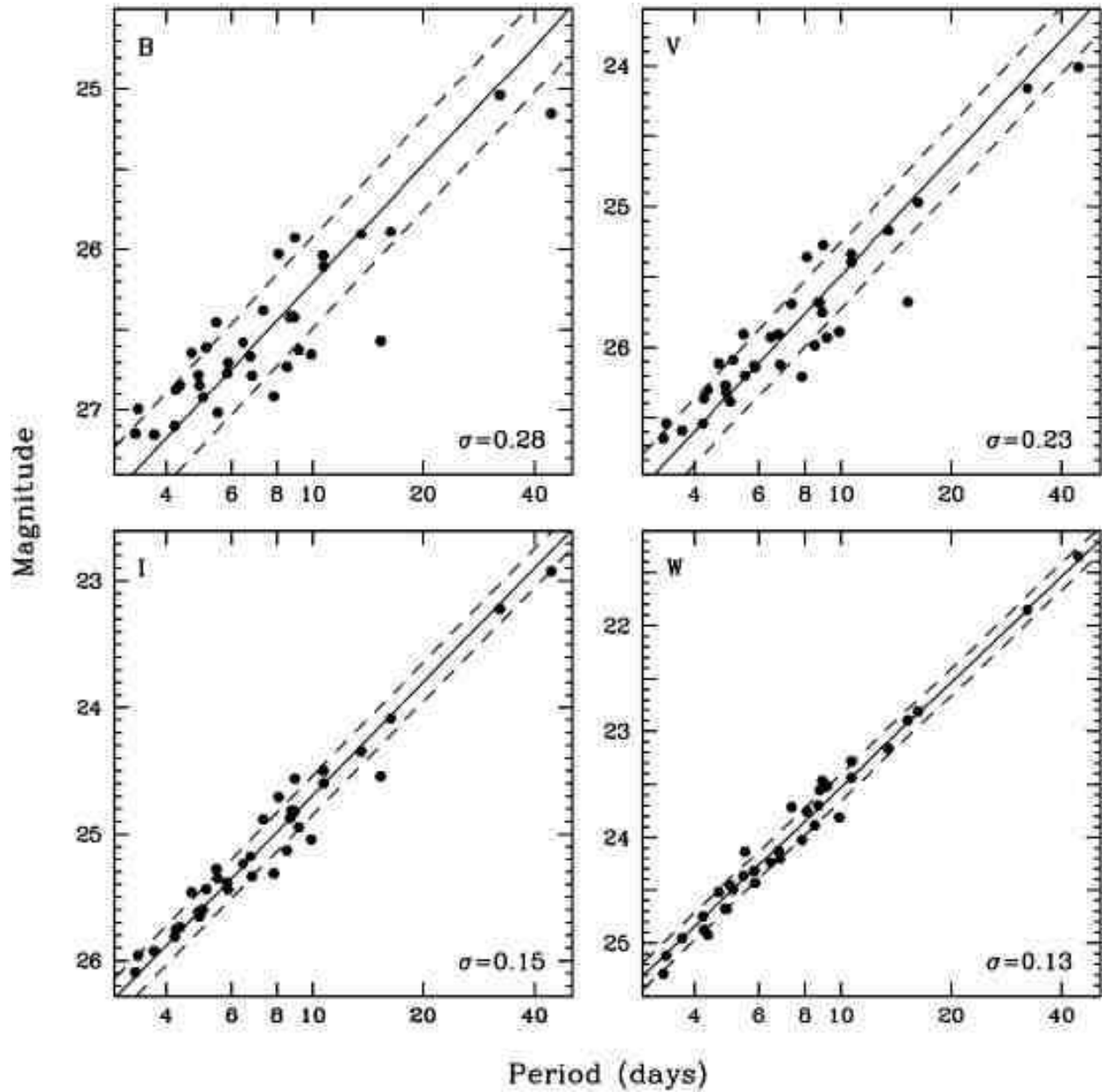


FIG. 13.— *BVI* and Wesenheit Period-Luminosity relations for the $L_V > 2$ sample of Cepheids in the outer field. The solid lines represent the LMC P-L relations derived by Udalski et al. (1999), shifted to the appropriate mean relative distance modulus. The dashed lines indicate the 1σ dispersion of the sample.

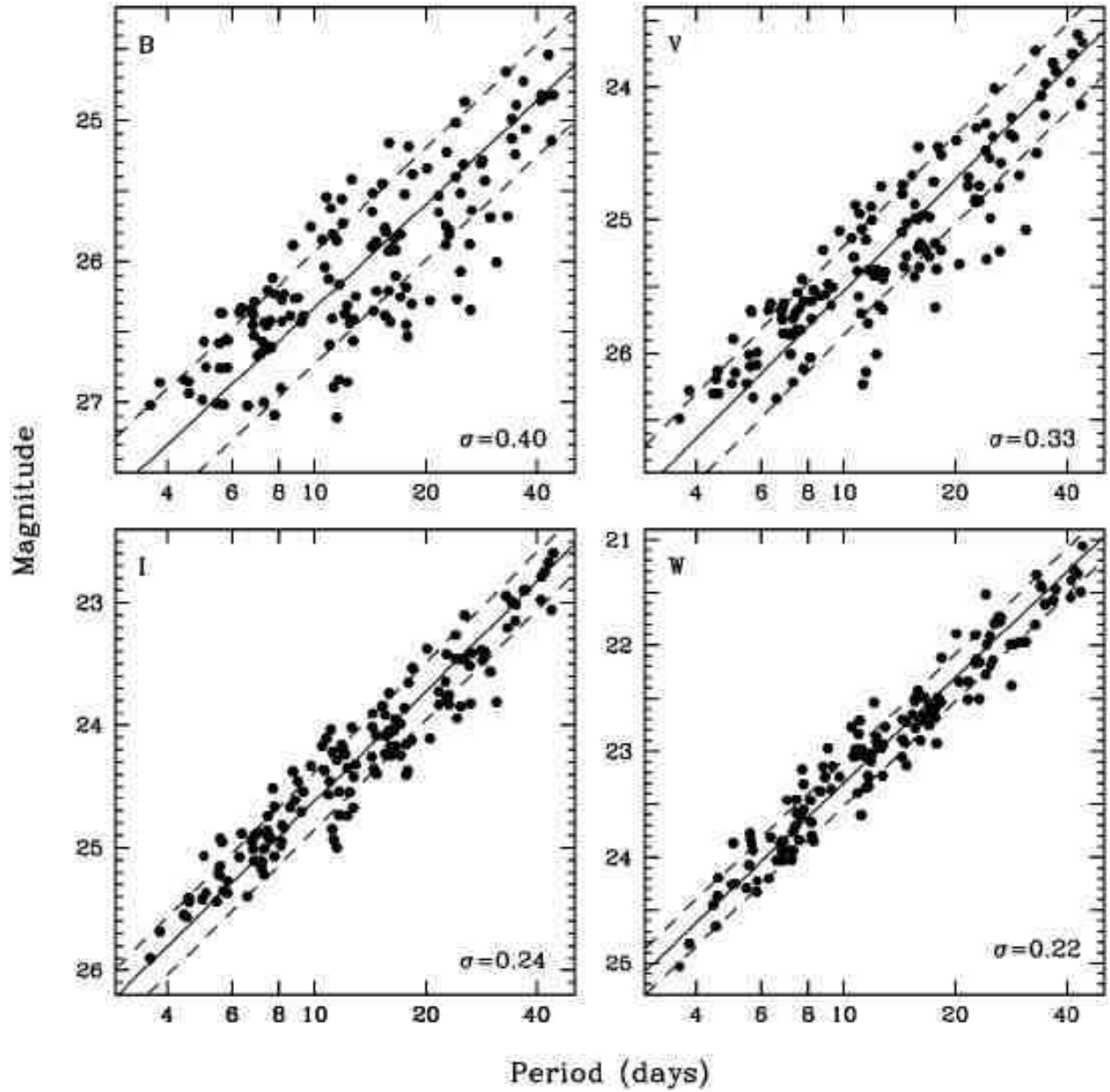


FIG. 14.— *BVI* and Wesenheit Period-Luminosity relations for the $L_V > 2$ sample of Cepheids in the inner field. The solid lines represent the LMC P-L relations derived by Udalski et al. (1999), shifted to the appropriate mean relative distance modulus. The dashed lines indicate the 2σ dispersion.

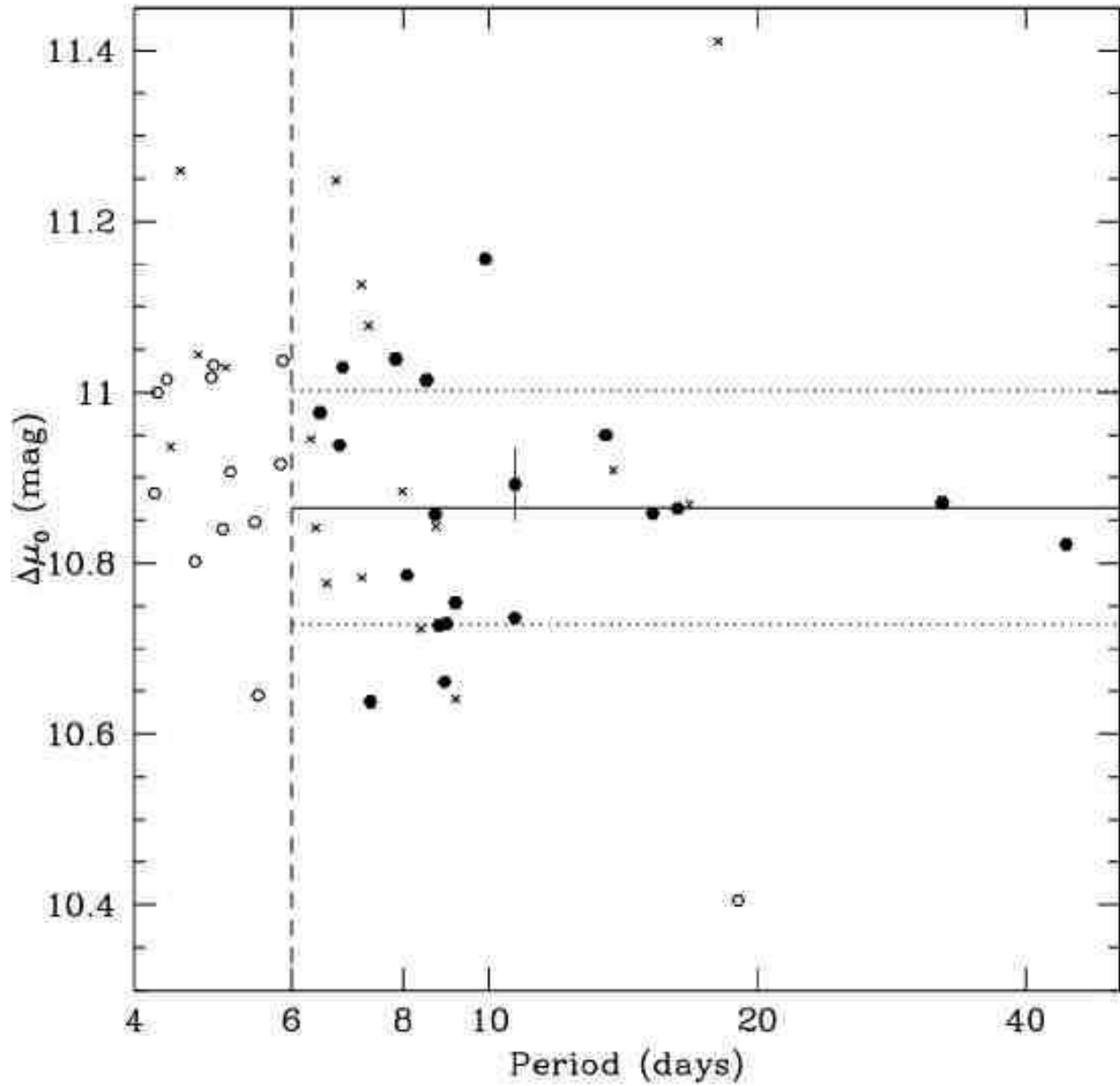


FIG. 15.— Relative distance modulus versus period for the restricted sample of Cepheids in the outer field. Crosses: Cepheid candidates that were rejected by selection criteria 1-4. Open circles: Candidates rejected by period cut or distance modulus clipping. Filled circles: Final sample of Cepheids used to determine the mean relative distance modulus. Solid line: mean relative distance modulus. Dotted lines: 1σ dispersion of the final sample. Dashed line: Final adopted period cut. A typical error bar is shown on one of the data points.

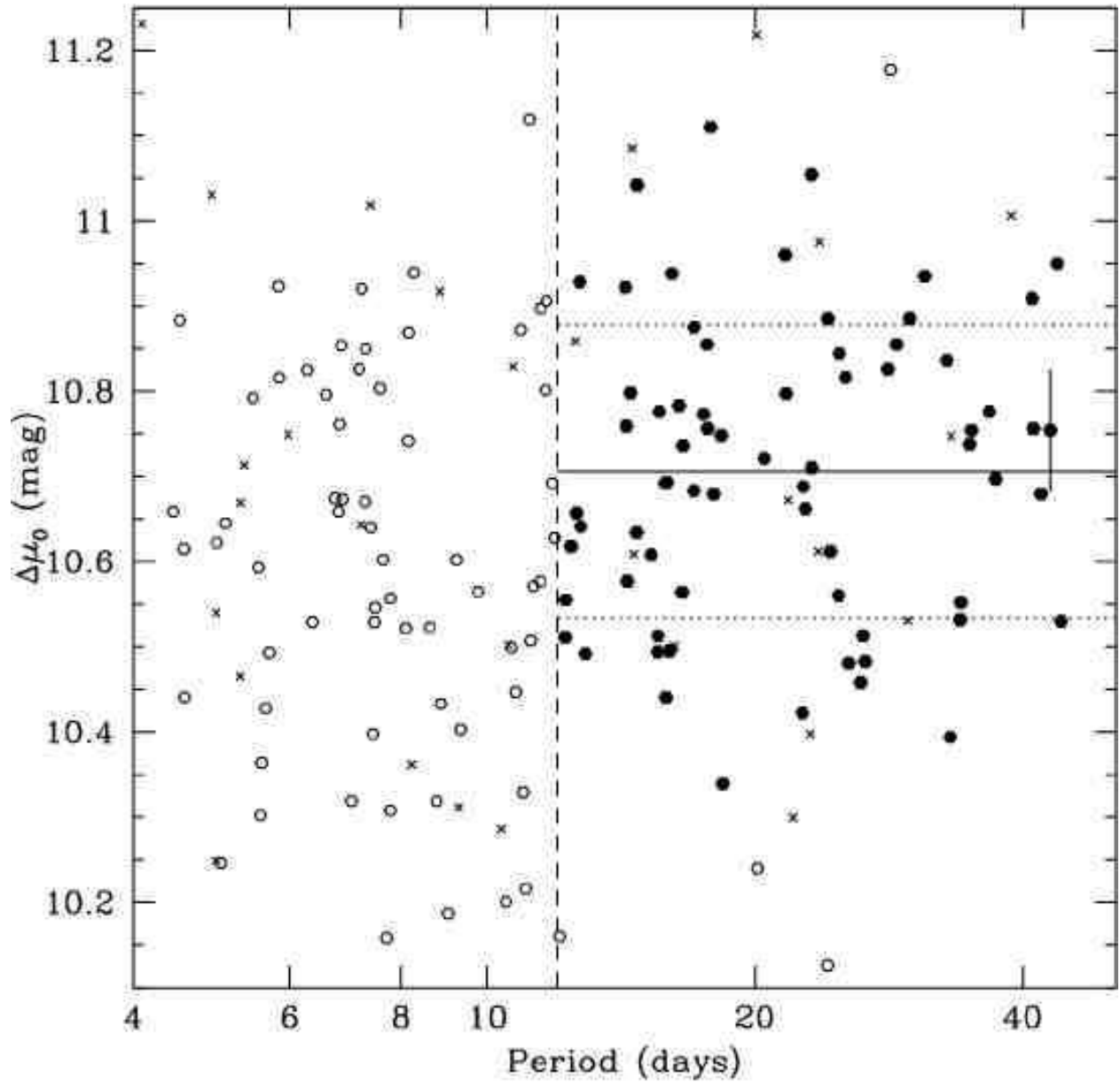


FIG. 16.— Relative distance modulus versus period for the restricted sample of Cepheids in the inner field. Crosses: Cepheid candidates that were rejected by selection criteria 1-4. Open circles: Candidates rejected by period cut or distance modulus clipping. Filled circles: Final sample of Cepheids used to determine the mean relative distance modulus. Solid line: mean relative distance modulus. Dotted lines: 1σ dispersion of the final sample. Dashed line: Final adopted period cut. A typical error bar is shown on one of the data points.

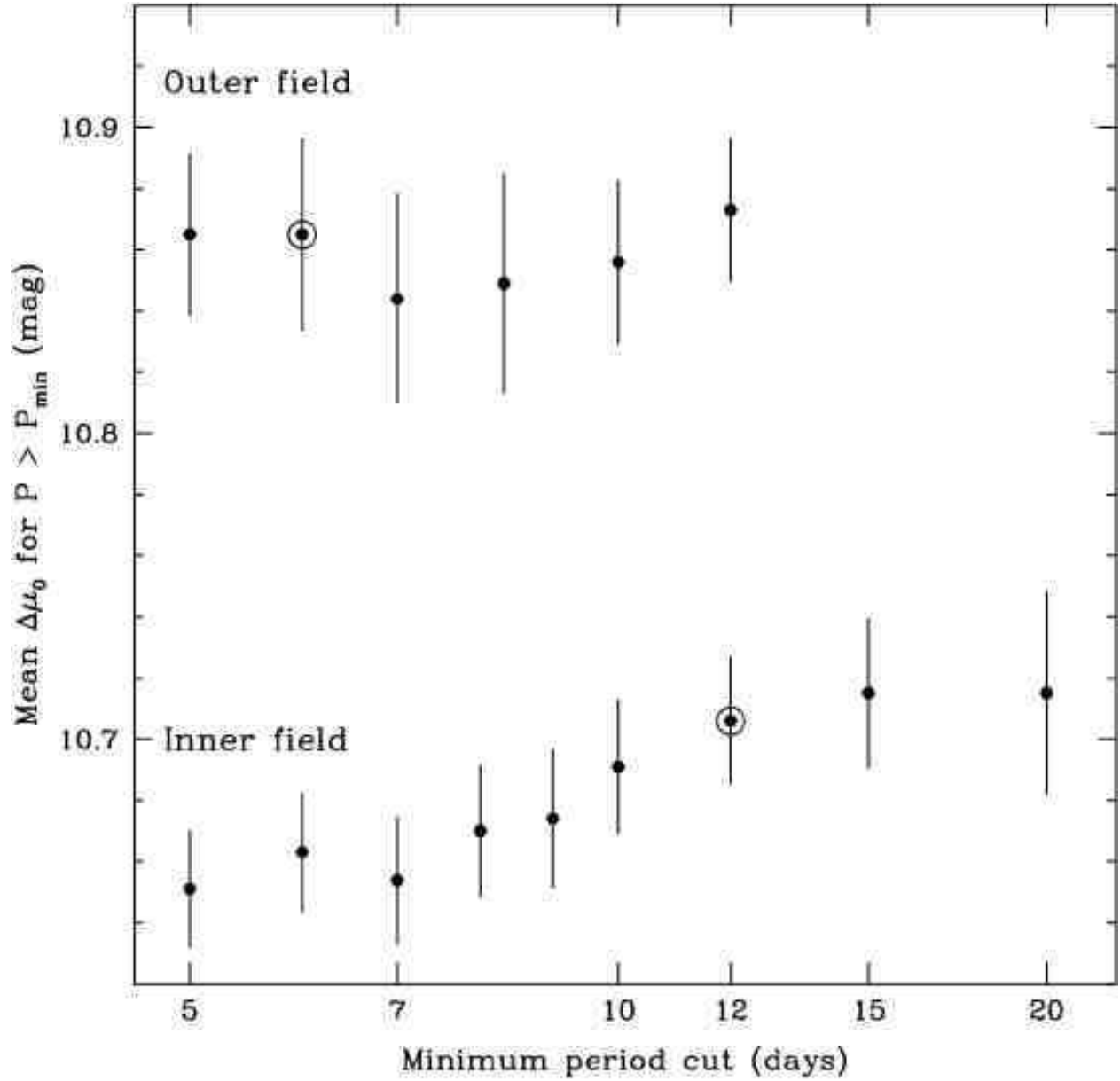


FIG. 17.— Mean distance modulus (relative to the LMC) as a function of cut at minimum period, for the $L_V > 2$ samples of the outer (top) and inner (bottom) fields. The error bars represent the 1σ uncertainty in the mean. Our final choices for minimum period cut are indicated with open circles.

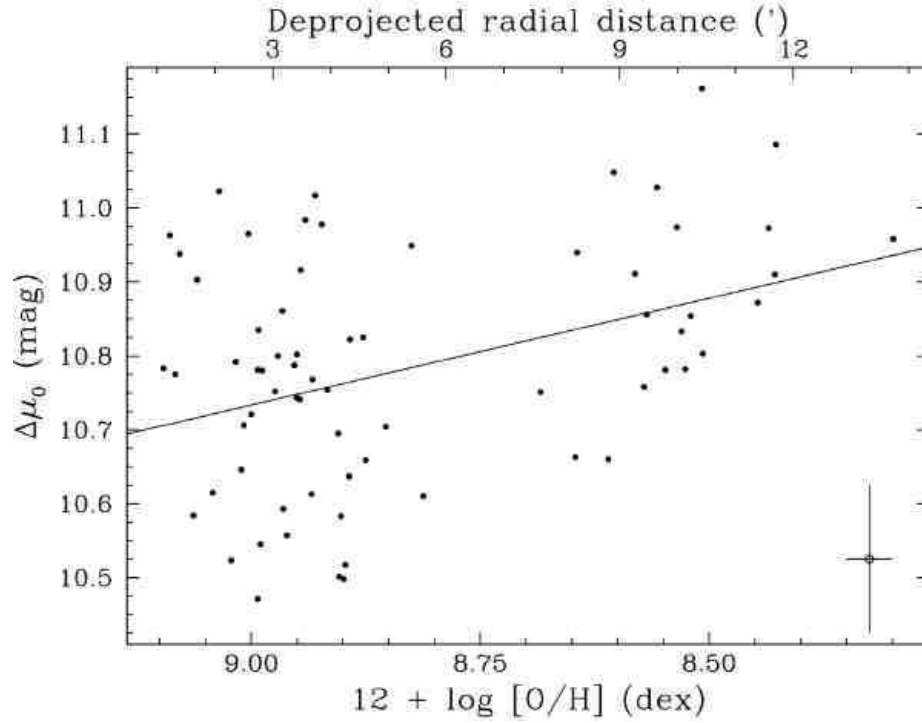


FIG. 18.— Correlation between distance moduli of individual Cepheids and their abundances, given by their galactocentric distances and the abundance gradient of Zaritsky et al. (1994). The best-fit line has a value of $-0.29 \pm 0.09_r \pm 0.05_s$ mag dex $^{-1}$. A representative individual uncertainty is shown on the open symbol in the bottom right.

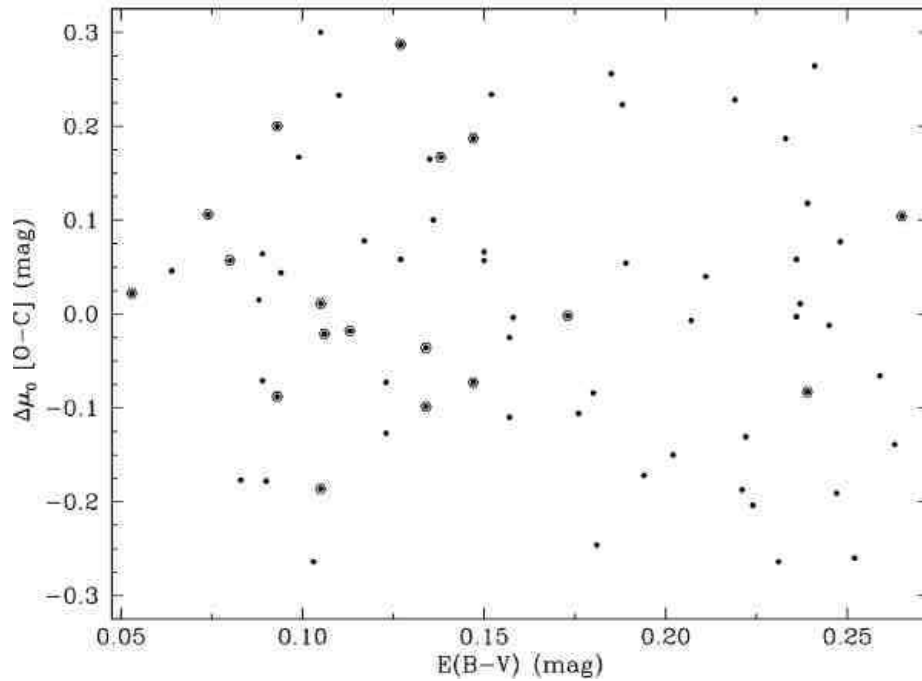


FIG. 19.— Residual of the individual Cepheid distance moduli about the best-fit line of Figure 18, plotted as a function of $E(B-V)$. Cepheids located in the outer field are represented by concentric open and filled symbols. Cepheids located in the inner field are indicated by filled symbols.

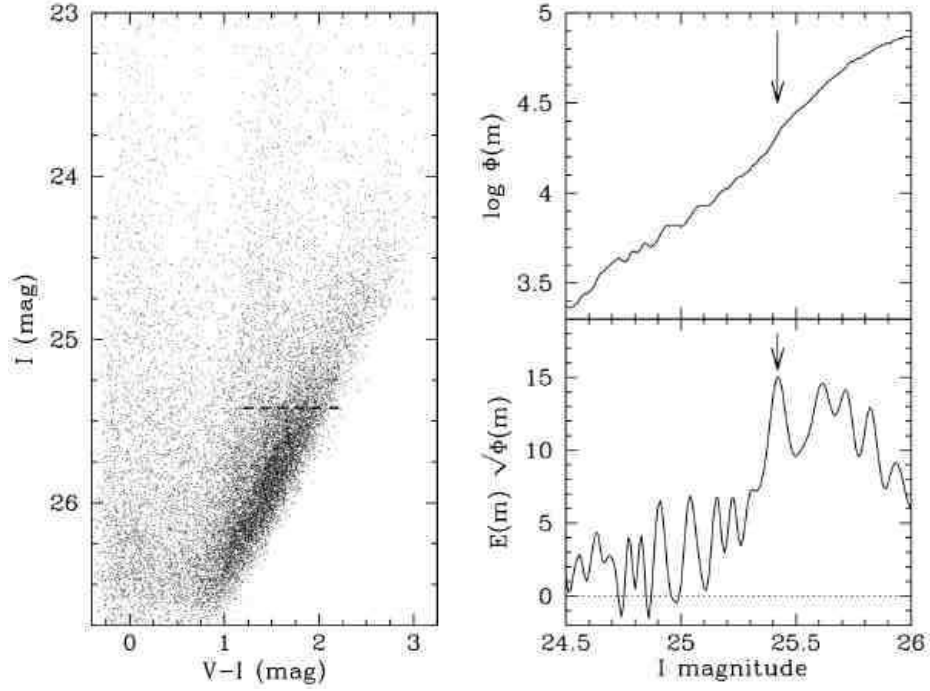


FIG. 20.— Determination of the I -band magnitude of the Tip of the Red Giant Branch in the outer field of NGC 4258. Left: I -band color-magnitude diagram, indicating the location of the TRGB (dashed line). Right: I -band luminosity function $\phi(m)$ and edge function $E(m)\sqrt{\phi(m)}$, indicating the detection of the TRGB edge at $I = 25.42 \pm 0.02$ mag.

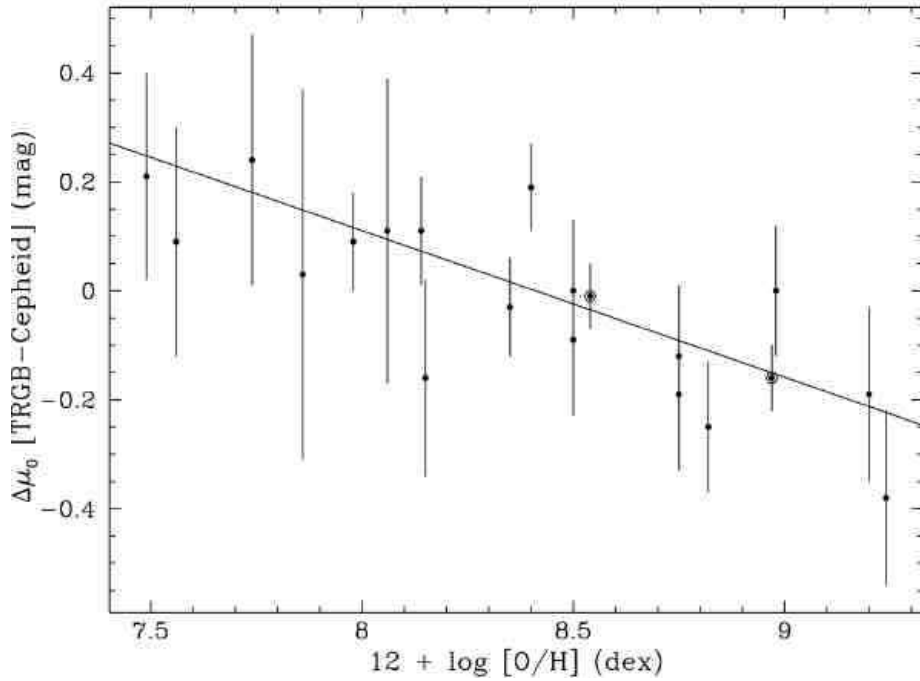


FIG. 21.— Cepheid metallicity dependence determined through a comparison of TRGB and Cepheid distance moduli for 20 fields in 18 galaxies. This Figure reproduces the bottom panel of Figure 12 of Sakai et al. (2004), with the addition of two points for our fields in NGC 4258, shown with concentric open and filled symbols.

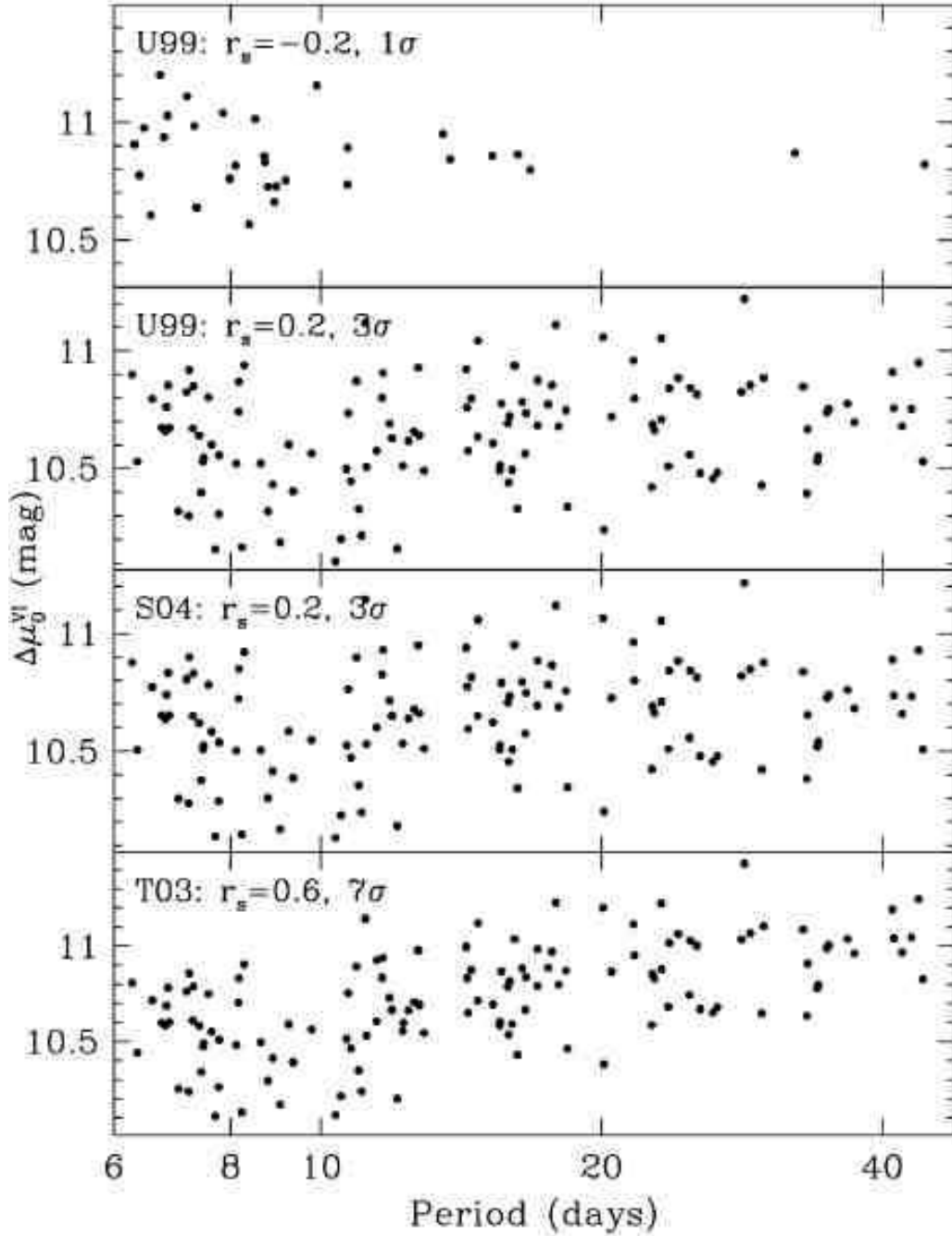


FIG. 22.— Correlation between period and extinction-corrected LMC-relative distance moduli for different choices of input P-L relation. Top panel: Outer field Cepheids. Bottom three panels: Inner field Cepheids. U99=Udalski et al. (1999); S04=Sandage et al. (2004); T03=Tammann et al. (2003). The LMC P-L relations are good fits to the Cepheid samples of both fields. The adoption of the Milky-Way P-L relations of Tammann et al. (2003) leads to a residual slope with a significance of $\sim 7\sigma$ level for $P_{min} = 6$ d or $\sim 4\sigma$ for $P_{min} = 12$ d.

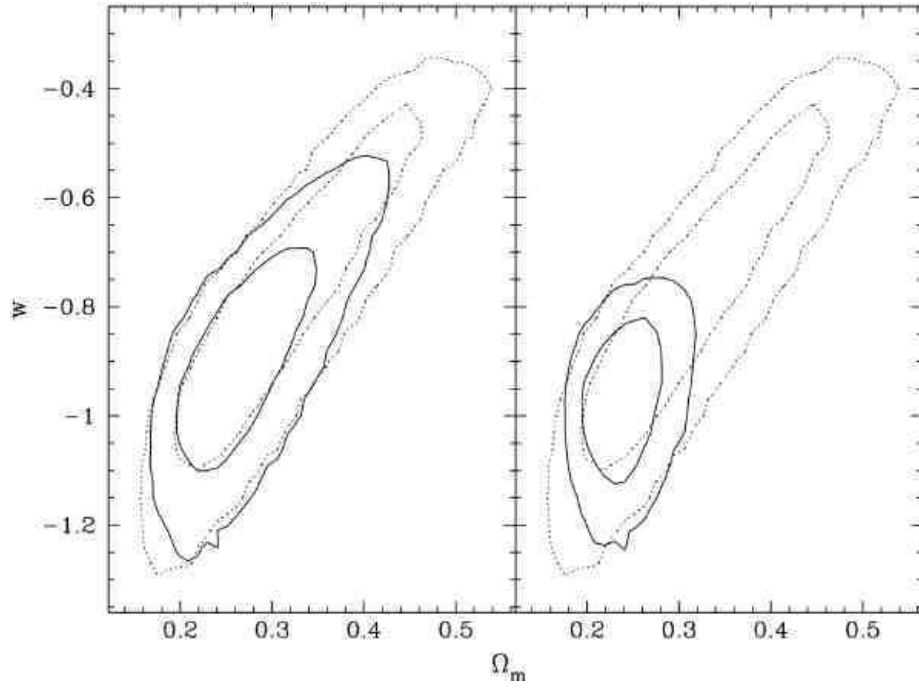


FIG. 23.— WMAP 3-year 1 and 2σ error contours (dashed lines) in the $\Omega_M - w$ plane, for the Λ CDM+ w model of Spergel et al. (2006). The solid contours represent the improvement obtained by using priors on H_0 . Left panel: prior of $H_0 = 72 \pm 7 \text{ km s}^{-1} \text{ Mpc}^{-1}$ (Freedman et al. 2001). Right panel: prior of hypothetical future measurement of $H_0 = 74 \pm 3.5 \text{ km s}^{-1} \text{ Mpc}^{-1}$.

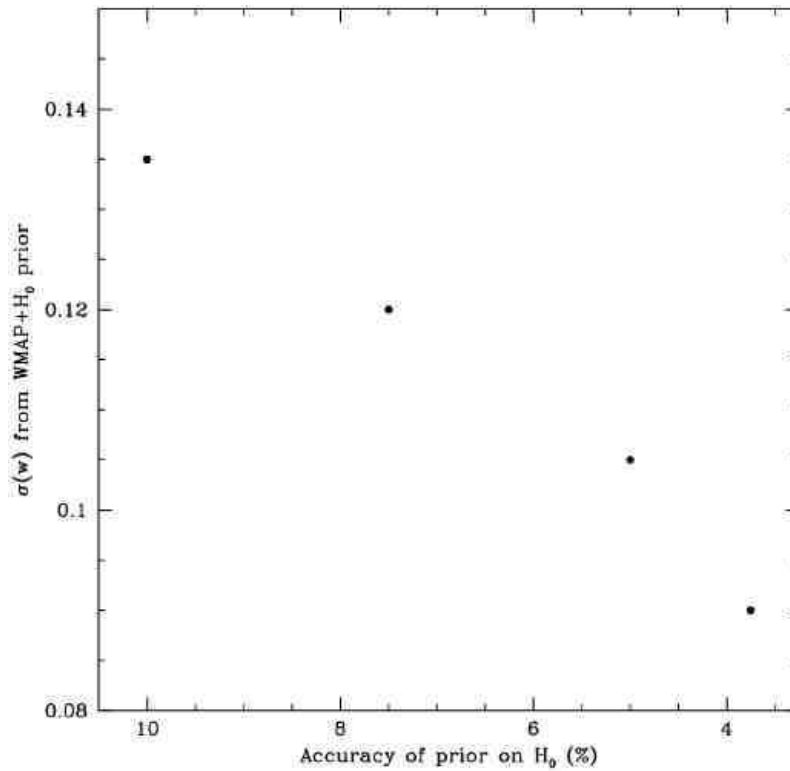


FIG. 24.— 1σ uncertainty in the value of w for the Λ CDM+ w model of Spergel et al. (2006), after including hypothetical priors on H_0 with a value of $74 \text{ km s}^{-1} \text{ Mpc}^{-1}$ and decreasing uncertainty.

TABLE 1
LOG OF OBSERVATIONS

Visit #	UT Date	MJD at mid exposure*					
		B	I	V	B	I	V
O-01	2003 December 6	2980.0640	0.0734	0.0823	0.1206	0.1300	0.1389
O-02	2003 December 7	2980.7980	0.8073	0.8163	0.8533	0.8627	0.8716

Table appears in its entirety in the full-resolution version of the paper

NOTE. — *: JD-2450000.0 for first exposure; thereafter, only the last five digits are given. †: Guide star problems; limited usefulness. O: outer field; I: inner field.

TABLE 2
SECONDARY STANDARDS

ID	R.A.	Dec.	X	Y	V	I	B
	(J2000.0)						
O-42521	12:19:12.170	47:10:55.12	3587.1	4181.2	23.203(10)	23.099(16)	23.275(05)
O-42199	12:19:12.218	47:10:48.86	3704.5	4137.1	23.171(07)	22.911(07)	23.367(06)

Table appears in its entirety in the full-resolution version of the paper

NOTE. — Uncertainties are given in parentheses and are expressed in units of 10^{-3} mag. O: outer field; I: inner field.

TABLE 3
EFFECTS OF SELECTION CRITERIA

Selection criteria (§3.3)	$L_V > 0.75$		$L_V > 2.0$	
	Inner	Outer	Inner	Outer
Initial Sample	402	134	195	63
1. Amplitude ratios	-110	-28	-23	-4
2. $E(B-V) < \text{foreground } (2\sigma)$	-37	-30	-17	-20
3. $E(B-V) > 0.5 \text{ mag}$	-9	-1	-6	-1
4. $\Delta\mu_0 > 12 \text{ mag} \ \& \ \sigma \text{ clipping}$	-28	-12	-11	-3
Final sample	218	63	138	35

NOTE. — This table shows the reduction in size of the different samples as a result of the selection criteria listed in §3.3.

TABLE 4
CEPHEID VARIABLES – BASIC DATA

ID	Per. (d)	R.A. (J2000.0)	Dec.	X (pixels)	Y (pixels)	V	Magnitudes		Amplitudes			L_V
							I	B	V	I	B	
O-15165	3.30	12:19:20.668	47:10:31.19	3567.3	2383.1	26.646(042)	26.092(040)	27.148(054)	503	168	691	2.01
O-21998	3.36	12:19:17.808	47:10:11.81	4100.5	2836.1	26.540(043)	25.959(043)	26.993(061)	482	214	812	2.26

Table appears in its entirety in the full-resolution version of the paper

NOTE. — Errors in mean magnitudes are shown in parenthesis and expressed in units of 10^{-3} mag. Light curve semi-amplitudes are expressed in units of 10^{-3} mag. O: outer field; I: inner field.

TABLE 5
REJECTED CEPHEID CANDIDATES

ID	Per. (d)	R.A. (J2000.0)	Dec.	X (pixels)	Y (pixels)	V	Magnitudes		Amplitudes			L_V
							I	B	V	I	B	
$N_V < 18$ or $N_I < 18$ or $N_B < 18$												
O-18637	3.21	12:19:21.128	47:11:27.81	2453.4	2607.1	27.000(051)	26.281(052)	27.409(077)	361	190	474	1.27
O-03121	3.23	12:19:27.280	47:10:20.74	3394.4	1030.0	27.158(030)	26.623(113)	26.981(027)	359	0	29	0.92

Table appears in its entirety in the full-resolution version of the paper

NOTE. — Errors in mean magnitudes are shown in parenthesis and expressed in units of 10^{-3} mag. Light curve semi-amplitudes are expressed in units of 10^{-3} mag. O: outer field; I: inner field.

TABLE 6
CEPHEID VARIABLES – DERIVED PROPERTIES

ID	Per. (d)	μ_0^{VI}	$E(V-I)$	μ_0^{av}	$E(B-V)$	r/r_{iso}
		(mag)	(mag)	(mag)	(mag)	
O-15165	3.30	11.009(115)	0.022(025)	11.009(075)	0.016(025)	1.30
O-21998	3.36	10.900(122)	0.022(025)	10.901(075)	0.016(025)	1.23

Table appears in its entirety in the full-resolution version of the paper

NOTE. — μ_0^{VI} : Extinction corrected distance modulus derived from V&I data (Eq. 7). μ_0^{av} : Extinction corrected distance modulus derived from the average of Eqns. (7-9). $E(B-V)$: Average value of extinction derived from all measured color excesses. Errors in distance moduli and extinction are shown in parenthesis and expressed in units of 10^{-3} mag. O: outer field; I: inner field.

TABLE 7
ERROR BUDGET OF THE CEPHEID DISTANCE SCALE

Error source	Previous	This work	Goal
A. Fiducial galaxy	LMC	NGC 4258	
S1. Distance modulus (sys)	0.13	0.12	0.04
R1. Distance modulus (ran)	...	0.09	0.02
B. Photometric calibration			
S2a. V zeropoint	0.03	0.02	0.02
S2b. I zeropoint	0.03	0.02	0.02
S2. Photometry (sys)	0.09	0.05	0.05
R2. Photometry (ran)	0.05	0.03	0.02
C. Extinction corrections			
R3. Uncertainty in R_V	0.02	0.02	0.02
R4. De-reddened PL fit	0.04	0.02	0.02
D. Metallicity corrections			
S3. Adopted correction	0.08	0.04	0.03
R_T . Total random	0.07	0.10	0.04
S_T . Total systematic	0.18	0.14	0.07
Combined error (mag)	0.19	0.17	0.08
Combined error (%)	10	8	4

NOTE. — All errors expressed in magnitudes unless otherwise indicated. Previous: adapted from Gibson et al. (2000). Goal: Anticipated reduction in uncertainties from Humphreys et al., (in prep.), Bersier et al., (in prep.) and Macri et al., (in prep.).

TABLE 8
UPDATED DISTANCE MODULI TO HIGH-QUALITY TYPE IA SNE

Galaxy name	SN	[O/H] (dex)	μ_0 (mag)	$\mu_{0,Z}$ (mag)	M_V^0 (mag)	Ref.
NGC 3370	1994ae	8.80 ± 0.05	32.23 ± 0.04	32.31 ± 0.06	-19.15 ± 0.12	R05
NGC 3982	1998aq	8.75 ± 0.05	31.56 ± 0.08	31.63 ± 0.09	-19.15 ± 0.12	S01
NGC 4536	1981B	8.85 ± 0.20	30.80 ± 0.04	30.90 ± 0.06	-19.18 ± 0.12	F01
NGC 4639	1990N	9.00 ± 0.20	31.61 ± 0.08	31.75 ± 0.09	-19.08 ± 0.12	F01
Average				$M_V^0 = -19.14 \pm 0.07$		

NOTE. — μ_0 : Published Cepheid distance moduli; $\mu_{0,Z}$: Distance moduli corrected for metallicity and our determination of the distance to the LMC. References: F01 = Freedman et al. (2001); R05 = Riess et al. (2005); S01 = Stetson & Gibson (2001).

TABLE 9
CEPHEID PHOTOMETRY

Visit	V	I	B	V	I	B	V	I	B
	O-15165 $P = 3.30$ d			O-21998 $P = 3.36$ d			O-10450 $P = 3.71$ d		
1	26.900(096)	26.247(165)	27.532(121)	26.878(183)	25.915(120)	27.575(117)	26.565(116)	25.775(154)	26.898(109)
2	26.797(163)	26.644(287)	26.448(325)	27.048(150)	26.091(208)	...	26.749(151)	26.068(123)	27.192(118)
3	27.160(118)	26.413(162)	27.715(199)	27.090(160)	26.795(260)	27.453(272)	26.981(232)	26.310(219)	27.634(181)
4	27.000(188)	26.367(161)	27.304(157)	27.178(207)	26.153(187)	27.661(365)	26.955(160)	26.114(163)	27.653(244)
5	26.118(073)	25.837(117)	26.391(076)	25.992(062)	25.825(114)	26.137(068)	26.912(091)	26.472(214)	27.912(236)
6	26.121(084)	25.973(144)	26.370(146)	25.942(089)	25.873(229)	26.199(104)	27.345(194)	25.990(117)	27.864(277)
7	27.430(268)	...	27.672(170)	26.683(115)	26.082(126)	27.116(139)	26.127(088)	25.901(191)	26.461(093)
8	26.994(198)	25.925(142)	27.453(167)	26.887(169)	26.252(180)	27.225(180)	26.268(083)	25.710(155)	26.591(144)
9	26.283(084)	25.768(083)	26.304(082)	26.033(098)	25.567(120)	26.242(072)	26.607(127)	26.262(250)	27.656(200)
10	25.882(135)	25.868(165)	26.605(093)	26.074(097)	25.677(095)	26.222(064)	27.255(166)	25.975(155)	27.197(212)
11	27.057(247)	26.516(307)	27.971(295)	27.290(340)	26.589(342)	28.269(270)	26.768(186)	25.892(163)	26.691(078)
12	27.188(139)	26.129(103)	27.722(315)	26.773(105)	26.177(132)	27.532(207)	26.223(044)	26.346(206)	26.622(091)
13	26.727(171)	26.342(221)	27.554(137)	26.749(111)	25.874(165)	27.785(287)	27.022(256)	26.507(205)	...
14	26.691(188)	25.951(117)	28.008(229)	26.812(142)	26.442(275)	27.492(234)	26.349(072)	25.814(135)	26.683(122)

NOTE. — The Julian Date for each visit can be found in Table 1. (*): Measurement deviated by more than 3σ from best-fit template light curve and was rejected. This table is available in its entirety upon request.